GUIDED-MODE RESONANT SOLAR CELLS AND FLAT-TOP REFLECTORS:

ANALYSIS, DESIGN, FABRICATION AND CHARACTERIZATION

by

TANZINA KHALEQUE

Presented to the Faculty of the Graduate School of

The University of Texas at Arlington in Partial Fulfillment

of the Requirements

for the Degree of

DOCTOR OF PHILOSOPHY

THE UNIVERSITY OF TEXAS AT ARLINGTON

May 2014

Acknowledgements

I am sincerely grateful to Almighty Allah for granting me all the opportunities and blessings to live a better life and conquer the highest degree in education. I convey my sincere appreciation and humble gratitude to my supervising professor Dr. Robert Magnusson for giving me the opportunity to work in “Nanophotonics Device Group”. His resourceful guidance, suggestions, encouragement and support have always been the motivation towards my research works.

I would like to thank Dr. Jonathan Bredow, Dr. Weidong Zhou, Dr. Michael Vasilyev, Dr. Cheng Luo and Dr. Halldor G. Svavarsson for their kind consent to be in my supervising committee. I respect their valuable suggestions and comments. It has been fortunate to work with Dr. Halldor in one of my research projects.

I would like to thank Dr. Jae W. Yoon, Wenhua Wayne and M. J. Uddin for their direct assistance, suggestions and cooperation in my different research projects. I am grateful to Dr. K. J. Lee for his laboratory trainings, information and support. I am also thankful to every member of Nanophotonics Device group for their advice, suggestions and comments through valuable discussions. Special thanks to Kristin. P. Bergfield for all the paper works regarding academic registration, conference attendance, journal submissions and experimental accessories purchases.

I would like to thank Dr. Nader Hozhabri, Dennis Bueno, and Richard K. Chambers for helping me in fabrication process optimization in nanofab facilities. Thanks to Dr. William E. Dillon, Gail Paniuski, and Ann Lewiston for different administrative help in the department.

Finally, I pay my sincere gratefulness to my parents Dr. Abdul Khaleque and Syeda Najma Khaleque who provided the environment, support and encouragement to build up my good academic standing. I am thankful to my parents-in-law who always

encouraged to my higher education. I am sincerely grateful to my husband Mohammad Jalal Uddin; without his support and help, I cannot even imagine my studies in USA. He was a mentor to my GRE preparation, applications and graduate studies. Last but not the least, thanks to my daughter Jinan Tazmeen Uddin for making my life so blissful and inspiring.

April 11, 2014

Abstract

GUIDED-MODE RESONANT SOLAR CELLS AND FLAT-TOP REFLECTORS:

ANALYSIS, DESIGN, FABRICATION AND CHARACTERIZATION

Tanzina Khaleque, PhD

The University of Texas at Arlington, 2014

Supervising Professor: Robert Magnusson

This dissertation addresses the guided-mode resonance (GMR) effect and its applications. In particular, this study presents theoretical analysis and corresponding experiments on two important GMR devices that can be broadly described as GMR-enabled thin-film solar cells and flat-top reflectors.

The GMR-induced enhanced absorption of input light is observed and quantified in a fabricated nano-patterned amorphous silicon (a-Si) thin-film. Compared to a reference homogeneous thin-film of a-Si, approximately 50% integrated absorbance enhancement is achieved in the patterned structure. This result motivates the application of these resonance effects in thin-film solar cells where enhanced solar absorbance is a crucial requirement. Light trapping in thin-film solar cells through the GMR effect is theoretically explained and experimentally demonstrated. Nano-patterned solar cells with 300-nm periods in one-dimensional gratings are designed, fabricated, and characterized. Compared to a planar reference solar cell, around 35% integrated absorption enhancement is observed over the 450–750-nm wavelength range. This light-management method results in enhanced short-circuit current density of 14.8 mA/cm^2, which is a ~40% improvement over planar solar cells. The experimental demonstration proves the potential of simple and well-designed guided-mode resonant features in thin-film solar cells.

In order to complement the research on GMR thin-film solar cells, a single-step, low-cost fabrication method for generating resonant nano-grating patterns on poly-methyl-methacrylate (PMMA; plexiglas) substrates using thermal nano-imprint lithography is reported. The imprinted structures of both one and two dimensional nano-grating patterns with 300 nm period are fabricated. Thin films of indium-tin-oxide and silicon are deposited over patterned substrates and the absorbance of the films is measured. Around 25% and 45% integrated optical absorbance enhancement is observed over the 450-nm to 900-nm wavelength range in one- and two-dimensional patterned samples, respectively.

In addition, two types of GMR flat-top reflectors have been designed, analyzed, fabricated and experimentally demonstrated. The first one is GMR broadband reflector in the spectral domain whereas the second is a Rayleigh reflector in the angular domain. The designed broadband reflector exhibits more than 99% reflectance over a spectral width of 380 nm ranging from 1440 to 1820 nm wavelength. Experimental reflectance greater than 90% is achieved over a ~360-nm bandwidth. The reported reflector bandwidth exceeds comparable published results for two-part periodic structures working in transverse electric polarization. In the Rayleigh reflector, the interaction of GMR and Rayleigh anomaly creates an extraordinary photonic response and results in a flat-top angularly delimited optical filter. The physical process of the rapid energy exchange between the reflected zero-order wave and a propagating substrate wave across a small angular change is investigated with numerical computations. An experimental proof of the Rayleigh reflector concept is presented. The combined GMR-Rayleigh anomaly effect holds the potential to portend a new research area of novel photonic devices with interesting and useful attributes.

Table of Contents

List of Illustrations

List of Tables

Chapter 1

Introduction

Guided-mode resonance (GMR) effects arise via quasi-guided, or leaky, waveguide modes induced on patterned films with subwavelength periods. Materials including dielectrics, semiconductors, and metals can be used to build GMR elements patterned in one or two dimensions. Nanopatterned resonance elements yield versatile spectra with a rich variety of possible surface-localized photonic states. On account of advances in design and fabrication, new aspects, attributes, and application possibilities continue to appear. The parametric design space allows control of light amplitude, phase, polarization, near-field intensity, and light distribution on surfaces as well as within the device volume. The desired output spectra can be retrieved in either transmission or reflection mode. There is a growing body of publications on these resonance effects [1-25]

In the literature, various different terms have been used to define the fundamental resonance effect. The term "guided-mode resonance" first appeared in 1990 to describe the resonance behavior in planar dielectric layer diffraction gratings [5]. Guided-mode resonance (GMR) or leaky-mode resonance (LMR) refers to a sharp peak in the diffraction efficiency spectrum of a waveguide grating structure associated with 100% energy exchange between reflected and transmitted waves. The periodic modulation of the waveguide's relative permittivity constitutes the phase-matching element to couple the externally propagating diffracted fields to the modes of the waveguide [6, 7]. Due to the periodic modulation of the guide, the structure is leaky in nature and thus the guided-modes cannot sustain on the waveguide grating. With device period and thickness on the order of the incident wavelength, the GMR elements yield versatile photonic spectra. Using powerful electromagnetic design methods, the spectral bands of these subwavelength resonant structures can be engineered to achieve photonic devices with efficient practical attributes. It has already been shown that a simple resonance layer enables narrow-line bandpass and bandstop filters [6, 7, 26-33], laser mirrors [6, 25, 34], polarizers [13, 20, 35], wideband reflectors [36-38], tunable filters [22, 23, 39-41], polarization-independent filters [13] and biosensors [42, 43]. This dissertation focuses on GMR applications in thin-film solar cells [44, 45] and analysis of the extraordinary capability of flat-top reflectors using combined effect of GMR and the Rayleigh anomaly [46, 47]. We note that these topics are but a fraction of the possible applications proposed thus far. To put this work in further perspective, we provide in Table 1-1 a partial listing of some of the application identified to date [48].

1.1 Basic Concepts of GMR Devices

In the simplest form, a GMR element consists of a single layer grating on a substrate. This single layer also serves as a waveguiding medium with effective refractive index greater than that of the cover and the substrate. The waveguide layer may also be accommodated with one or multiple homogeneous layers in between the grating structure and the substrate. A guided-mode resonance occurs when one of the diffracted waves generated by the grating element is phase-matched to a leaky mode admitted by the waveguide structure [5-7].

Figure 1-1 shows schematic view of a GMR element with an obliquely incident plane wave and corresponding forward and backward diffracted waves. The grating layer consists of a high-index material n_H and a low-index material n_L; n_s and n_c are the refractive indices of the substrate and cover respectively. The characteristic parameters are denoted as period Λ, fill factor F, and grating depth d_g.

Table 1-1 Applications Enabled by the Guided-Mode Resonance Effect

• **Frequency selective elements** - Narrowband bandstop/bandpass filters ($\Delta\lambda$ ~sub nm) - Wavelength division multiplexing (WDM) - Ultra high-Q thin-film resonators - Laser resonator frequency selective mirrors
• **Biochemical sensors** - Spectroscopic biosensors - Chemical and environmental sensors - Multiparametric biosensors (biolayer thickness, refractive index, and background in a single measurement)
• **Wideband lossless mirrors** - Wideband bandstop/bandpass filters ($\Delta\lambda$ ~100's nm) - Mirrors for vertical-cavity lasers - Omnidirectional reflectors
• **Polarization control elements** - Polarization independent reflection/transmission elements for both 1D and 2D periodicity - Narrow or wideband polarizers - Non-Brewster polarizing laser mirrors - Polarization control including wave plates
• **Tunable elements** - Tunable filters, EO modulators, and switches - Liquid-crystal integrated tunable devices - Laser cavity tuning elements - MEMS-tunable display pixels and filters - Thermally tuned silicon filters
• **Security devices** - Resonant Raman templates - Compact non-dispersive spectroscopy
• **Thin-film light absorbers** - Absorbance-enhanced solar cells - Omnidirectional, wideband, polarization-independent absorbers - GMR coherent perfect absorbers
• **Photonic metasurfaces** - Wavefront-shaping elements including focusing reflectors
• **Dispersive elements** - Slow-light/dispersion elements
• **Hybrid resonant elements** - Leaky-mode nanoplasmonics - Hybrid plasmonic/modal resonance sensors - Rayleigh reflectors with sharp angular cutoff - Rayleigh-anomaly based GMR transmission filters

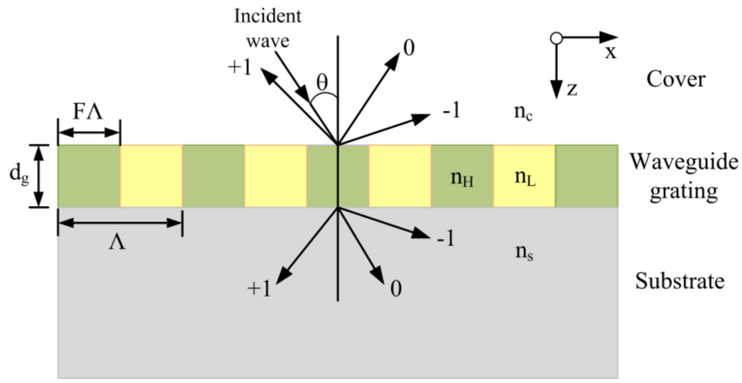

Figure 1-1 A basic single layer waveguide grating GMR element; Λ indicates grating period, F denotes fill factor, d_g is the grating thickness, θ is the angle of incidence, and n represents the refractive indices of the various regions.

When a plane wave is incident on the waveguide grating, it is divided into multiple diffracted orders. The diffracted orders that satisfy the phase matching condition get coupled into the waveguide layer. The coupled-wave equations governing the field distribution inside the rectangular grating region can be expressed as [7, 49],

$$\frac{dE_i^2(z)}{dz^2}+\left[k_0^2 n_g^2-k_0^2\left(n_c\sin\theta-i\lambda/\Lambda\right)^2\right]E_i(z)+k_0^2\Delta\varepsilon\sum_{h=1}^{\infty}\frac{\sin(h\pi f)}{h\pi}\left[E_{i-h}(z)+E_{i+h}(z)\right]=0 \tag{1.1}$$

where $E_i(z)$ is the y-component of the electric field amplitude of the i'th order diffracted wave, $k_0=2\pi/\lambda$, λ is the free-space wavelength, n_g is the average refractive index of the grating layer, θ is the indent angle, $\Delta\varepsilon=n_H^2-n_L^2$ is the modulation strength, i is the integer diffracted order index, and h is the integer Fourier harmonic index.

When the modulation is weak $(\Delta\varepsilon\to 0)$, the coupling term becomes negligibly small and coupled-wave equation (1.1) reduces to,

$$\frac{dE_i^2(z)}{dz^2}+\left[k_0^2 n_g^2-k_0^2\left(n_c\sin\theta-i\lambda/\Lambda\right)^2\right]E_i(z)=0 \tag{1.2}$$

The wave equation associated with an unmodulated dielectric waveguide is given by [7],

$$\frac{dE^2(z)}{dz^2}+\left[k_0^2 n_g^2-\beta^2\right]E(z)=0 \tag{1.3}$$

where β is the propagation constant of the mode supported by the structure. A guided wave can be excited if the effective refractive index $N=\beta/k_0$ is in the range [7],

$$\max\{n_c,n_s\}\le|N|<n_g$$

From direct comparison between equations (1.2) and (1.3), the effective mode propagation constant corresponding to the i'th order evanescent diffracted wave is obtained as,

$$\beta\rightarrow\beta_i=k_0\left(n_c\sin\theta-i\lambda/\Lambda\right) \tag{1.4}$$

with an effective refractive index $N_i=\beta_i/k_0$. Equation (1.4) is the necessary phase matching condition to couple an evanescent diffracted order to a waveguide propagating mode. If the $i=+1$ and/or -1 order is phase matched to a waveguide mode, the amplitude of this leaky mode can become large enough to strongly couple to zero-order propagating waves and a GMR occurs with a complete energy exchange between the reflected and transmitted waves. If there is a constructive interference for the reflected waves and consequent destructive interference in the transmitted waves, the device works as a reflection filter and 100% reflection occurs at the resonance wavelength. An example spectrum associated with the GMR effect in a high-spatial-frequency single layer waveguide grating structure is shown in Figure 1-2 [29]. The device parameters are

Λ = 383 nm, F = 0.5, d_g = 166 nm, n_c = 1, n_s = 1.52, n_H = 2.0 and n_L = 1.8. For transverse electric (TE: electric field vector being perpendicular to the plane of incidence) polarized normally incident light, a GMR occurs at the 631-nm wavelength. However, a corresponding homogeneous layer with refractive index equal to the average refractive index of the grating layer does not show such spectral signature, as shown with dashed line in Figure 1-2; there is a striking difference in the pertinent spectra. In this work, we use rigorous coupled-wave analysis (RCWA) for the computations [49].

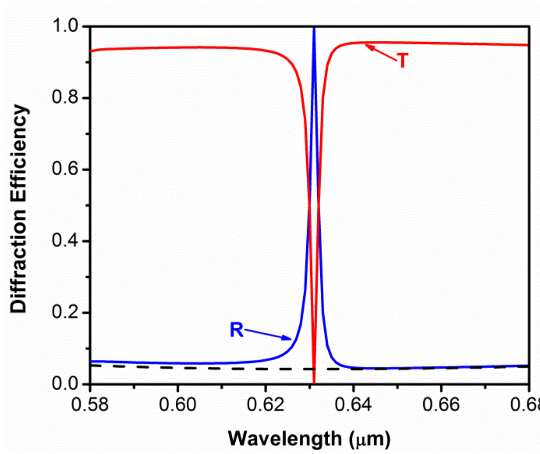

Figure 1-2 GMR effect in single layer waveguide grating structure. The parameters are Λ = 383 nm, F = 0.5, d_g = 166 nm, n_c = 1, n_s = 1.52, n_H = 2.0 and n_L = 1.8. The GMR occurs λ= 631 nm for TE polarized light with $\theta=0^o$. The dashed line represents the reflectance of the equivalent homogeneous layer with refractive index equal to the average refractive index of the grating layer.

1.2 Organization of the Dissertation

This study presents design, fabrication, and characterization of GMR elements applied in thin-film solar cells and flat-top reflectors. Chapters 2, 3 and 4 are dedicated to GMR thin-film photovoltaic applications. Chapters 5 and 6 include GMR wideband reflectors and Rayleigh reflectors, respectively.

Chapter 2 investigates GMR effect in lossy media. GMR-induced enhanced absorbance is observed in nano-patterned amorphous silicon thin films. Approximately 50% enhanced integrated absorbance is experimentally obtained compared to a reference planar thin-film silicon. Fabrication of nano-grating patterns with periods near 300 nm and ~60 nm grating depths in silicon films is described.

Chapter 3 demonstrates light management based on induced resonance effects in thin-film hydrogenated amorphous silicon (a-Si:H) solar cells. Integrated absorbance enhancement of about 35% is observed in nano-patterned GMR solar cells which led to ~40% enhanced photocurrents as compared to planar solar cells.

Chapter 4 introduces a fabrication approach of nano-structures using thermal nano-imprint lithography. The fabricated one and two dimensional structures on plexiglas substrate exhibit 300 nm periods with 60-70 nm grating depths. Deposited silicon films over these nano-patterned substrates exhibit enhanced absorption since the nano-structures induce GMR effect in the patterned films.

Chapter 5 reports design and fabrication of wideband GMR reflectors operating in TE polarization. The designed broadband reflector exhibits more than 99% reflectance over a spectral width of 380 nm across the 1440 to 1820 nm wavelength range. Experimental reflectance greater than 90% is achieved over ~360 nm bandwidth.

Chapter 6 describes the extraordinary behavior of Rayleigh reflectors with numerical analysis and also provides experimental verification of the concept. The combined effect of the GMR and the Rayleigh anomaly results in a flat-top reflector in angular spectra with sharp energy exchange between reflected and propagating waves.

Chapter 7 discusses the future research directions based on the work presented herein.

Chapter 2

GMR-Enabled Enhanced Absorption in Nano-Patterned Silicon Films

GMR enabled enhanced light absorption is demonstrated in a thin-film of amorphous silicon (a-Si) over glass substrate. One-dimensional nanoscale patterns with a period of 300 nm and a grating depth of 60 nm are fabricated on a-Si thin film, and their absorbance is compared with that of homogenous reference layers. Around 50% integrated absorption enhancement compared to unpatterned silicon reference samples is observed for the 400–950-nm wavelength range.

2.1 Introduction

Effective light trapping in thin-film solar cells is essential to improve their efficiency while contributing to the economic use of valuable silicon feedstock. Preliminary research results show engineered nanopatterns combined with minimal material expenditures are promising. In past work, diffraction gratings substantially affect light-absorption control in thin-film solar cells [1-4]. In order to increase optical path lengths in an active layer, random texturing, one- and two-dimensional photonic-crystal back reflectors, and patterned top antireflection layers have been studied [5-10]. Simulation results [2-4] show significant improvement of solar absorption, but actual high-quality fabrication of nano-scale patterns remains challenging with much added development required.

In this chapter, enhanced light absorbance in guided-mode resonant periodic thin-films is demonstrated theoretically and experimentally. One-dimensional patterns with a period of 300 nm and a grating depth of 60 nm are fabricated, and their absorbance is compared with that of homogenous reference layers. Considerable enhancement in light absorption is experimentally observed. The fabricated nano-patterns holds promising applicability in thin-film solar cells to enhance solar uptake.

2.2 GMR in Lossy Media

A subwavelength periodic pattern and a waveguide layer over a substrate constitute a generic GMR element, as shown in Figure 2-1(a), with characteristic parameters, period Λ, grating depth d_g, waveguide layer thickness d_{wg}, fill factor F, incident beam I, reflected beam R, and transmitted beam T. At resonance, an incident light beam couples to leaky waveguide modes through the grating structure. An efficient energy exchange occurs between the reflected and transmitted waves, resulting in sharp peaks in the diffraction efficiency spectrum of the resonant waveguide grating [11-13].

The grating couples the incident wave into the resonant waveguide-grating structure. A resonance occurs when one of the diffracted waves generated by the grating element phase matches to a leaky waveguide mode admitted by the waveguide structure, as schematically depicted in Figure 2-1(b). At the phase-matching condition, the effective mode propagation constant β_i, corresponding to the i-th order evanescent diffracted wave, is given by [13]

$$\beta_i = k_o(n_c \sin\theta_{in} - i\lambda / \Lambda) \tag{2.1}$$

where $k_0 = 2\pi/\lambda$, λ is the free space wavelength, n_c is the refractive index of cover medium, θ_{in} is the incident angle, and Λ is the period of the grating. The refractive index of the waveguide (n_{wg}) should be such that $n_{wg} > n_c, n_s, n_g$; where n_s is the refractive index of substrate and n_g is the average refractive index of the grating layer.

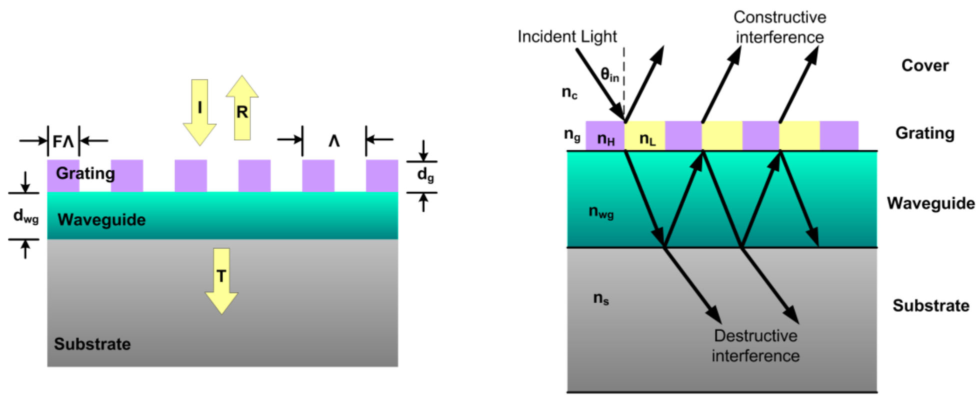

(a) (b)

Figure 2-1 (a) Schematic view of a GMR element featuring period Λ, grating depth d_g, waveguide thickness d_{wg}, and fill factor F, (b) schematic GMR coupling at resonance according to the model provided by Rosenblatt et al. [14].

Depending on the device parameters, operating wavelength, and incident angle, there can be a single resonance or multiple resonances. Using powerful electromagnetic design methods, the spectral bands of these resonant leaky-mode elements can be engineered for various photonic device applications. For example, it has already been shown that a single periodic layer with one-dimensional periodicity enables narrow line filters, polarizers, reflectors, and polarization-independent elements [15]. An example spectral response of a single-resonance device is shown in Figure 2-2. For the computations, we use a computer code based on rigorous coupled-wave analysis (RCWA) [16], which is a proficient algorithm to evaluate diffraction efficiency of periodic structures. In our numerical simulations, we use 11 harmonics; we verify good convergence by test simulations using 21 harmonics. For a simple waveguide-grating structure [17] with Λ = 280 nm, d_g = 55 nm, d_{wg} = 110 nm, F = 0.5, $n_{wg} = n_H$ = 2.02, $n_c = n_L$ = 1, and n_s = 1.5, a complete energy exchange occurs between transmitted and reflected waves and a sharp resonance reflectance peak occurs at the 487-nm wavelength when illuminated with normally incident transverse-electric (TE: electric field vector being orthogonal to the plane of incidence) polarized light. On the contrary, a homogeneous layer with an effective refractive index of the grating layer does not exhibit such spectral signature, as evidenced by dashed lines in Figure 2-2.

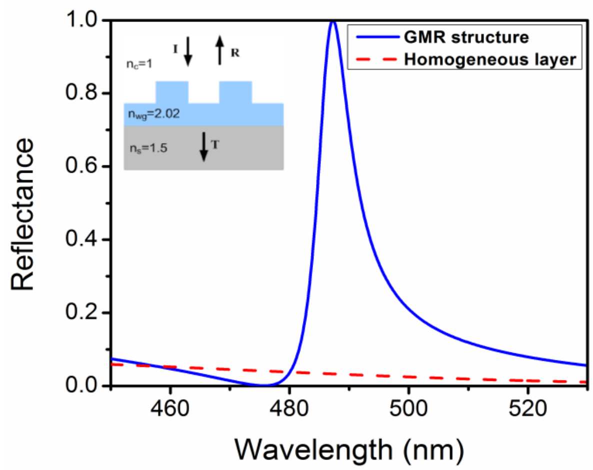

Figure 2-2 GMR spectral response of a waveguide-grating structure with Λ = 280 nm, d_g = 55 nm, d_{wg} = 110 nm, F = 0.5, $n_{wg} = n_H$ = 2.02, $n_c = n_L$ = 1, and n_s = 1.5. The GMR occurs at the 487-nm wavelength with TE polarized normally incident light. The dashed line represents the reflectance of a corresponding homogeneous layer with the grating replaced by a simple layer with an effective refractive index.

However, the GMR effect is strongly sensitive to material loss. Presence of material loss (complex refractive index N = n + iκ, where κ is the extinction coefficient) diminishes the external signatures of the resonance. If κ = 0.05 is considered in the previous example ($n_{wg} = n_H$ = 2.02 + i0.05), the reflectance decreases significantly, as depicted in Figure 2-3. The total internal electric field distributions of these elements for both lossless and lossy materials are shown as insets in Figure 2-3. We observe that even though the reflectance decreases, the field distribution with loss maintains key features with lower field levels. This shows that the field-enhancement aspect of the GMR effect can be beneficial without the traditional external signatures being present. If we compare the absorbance with a planar reference, an enhancement ratio of around 2.3 is obtained at the resonance wavelength, as shown in Figure 2-4.

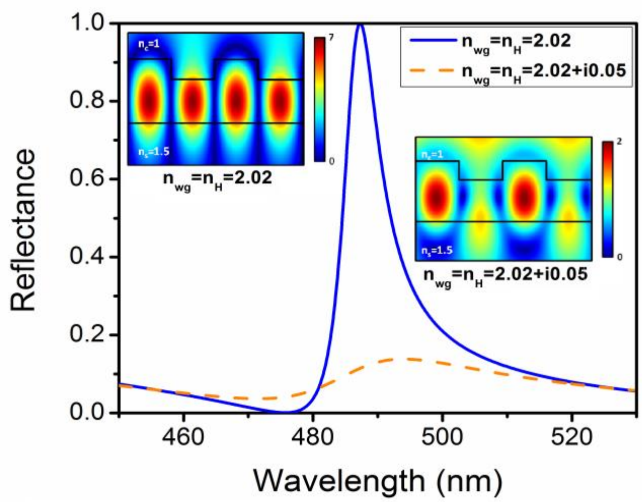

Figure 2-3 GMR spectral response of a waveguide-grating structure with Λ = 280 nm, d_g = 55 nm, d_{wg} = 110 nm, F = 0.5, n_c = n_L = 1, and n_s = 1.5. The solid line represents the GMR effect for lossless material where n_{wg} = n_H = 2.02, and the dashed line represents the reduced reflectance for lossy material where n_{wg} = n_H = 2.02 + i0.05. The total internal electric field distributions for both lossless and lossy materials at the resonance wavelength of 487 nm are shown as figure insets.

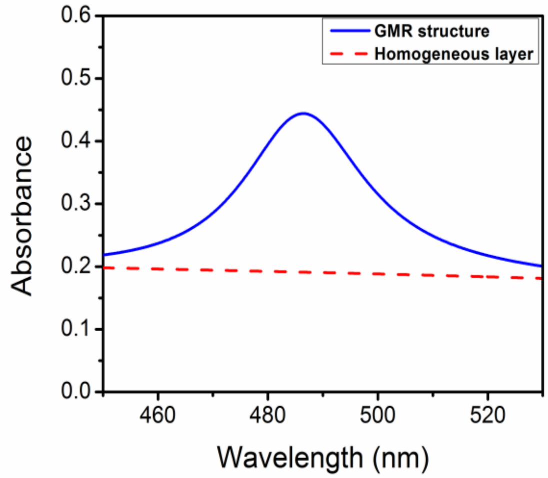

Figure 2-4 The solid line represents TE polarized absorbance spectra of a GMR structure with Λ = 280 nm, d_g = 55 nm, d_{wg} = 110 nm, F = 0.5, $n_c = n_L = 1$, $n_s = 1.5$, and $n_{wg} = n_H$ = 2.02 + i0.05. The dashed line represents the absorbance of a corresponding homogeneous layer with κ = 0.05. The absorbance is 2.3 times greater for the GMR element at the resonance wavelength of 487 nm.

2.3 Fabrication of Nano-Patterned Silicon Films

Amorphous silicon film with 570-nm thickness is deposited over clean glass substrate by sputtering. The thickness is measured by an Alpha-Step IQ surface profiler. Bottom antireflection coating, BARC (DUV30J-6), of 80 nm and photoresist (SEPR-701) of 240 nm are spin coated over the amorphous silicon. A laser interferometer with a 266-nm wavelength is used to transfer a one-dimensional grating pattern with a 300-nm period to photoresist by laser interferometric lithography. BARC from opening area is removed by reactive ion etching (RIE). The silicon is etched using a sulfur-hexafluoride (SF_6) and oxygen (O_2) gas mixture. The remaining photoresist and BARC layers are removed by RIE. Schematic view of the fabrication steps are summarized in Figure 2-5.

The image of the fabricated pattern taken with an atomic force microscope (AFM) is shown in Figure 2-6. From the figure, Λ = 302 nm, d_g = 60 nm, and F = 0.5.

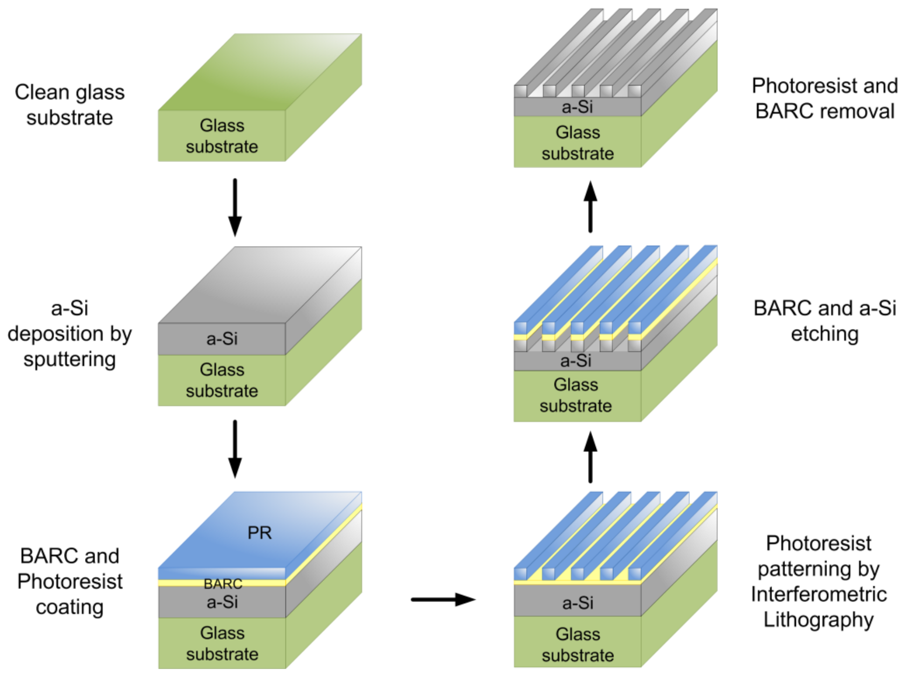

Figure 2-5 Schematic view of nano-patterned silicon film fabrication steps.

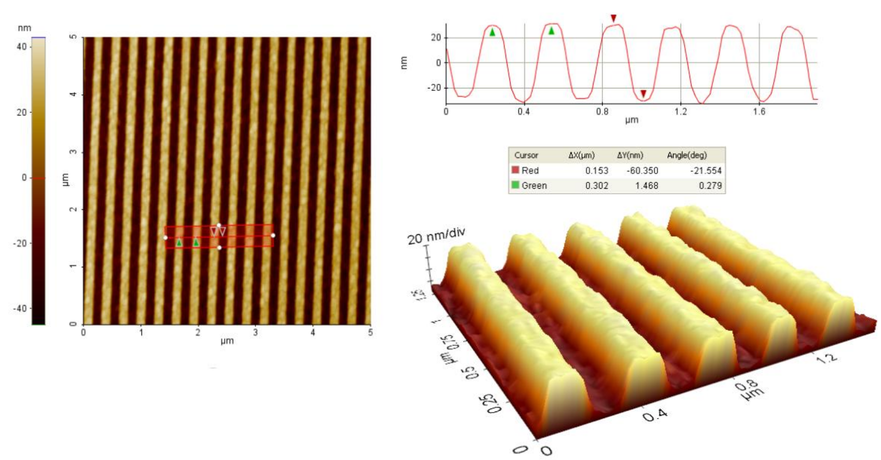

Figure 2-6 AFM image of fabricated nano patterned amorphous silicon film where Λ = 302 nm, d_g = 60 nm, and F = 0.5.

2.4 Results and Discussion

An Ocean Optics USB4000 fiber optic spectrometer is used to measure the reflected and transmitted light associated with these patterned amorphous silicon elements. Figure 2-7 shows schematic view of the transmission and reflection measurement setup through and from the devices respectively. In transmission measurement, light is directed to the sample through beam splitter and the light through the sample is detected by a detector. In reflection measurement, the reflected light from sample passes through the beam splitter to the detector.

The same measurements are conducted on a corresponding homogeneous layer of amorphous silicon to show the comparison. Figures 2-8 (a) and (b) show the transmitted, reflected, absorbed, and source (halogen lamp) spectra from the patterned and unpatterned silicon, respectively. The Rayleigh wavelength for the patterned structure is 450 nm. Beyond 450 nm, only zero-order diffraction prevails. Reflectance and transmittance spectra normalized to the source spectrum are measured from the data shown in Figure 2-8 (a,b), and absorbance is obtained as A = 1-R_0-T_0. Figure 2-9 shows the comparison of absorbance between patterned and unpatterned silicon. Integrated absorbance enhancement of about 50% is measured over 400-950 nm wavelength range.

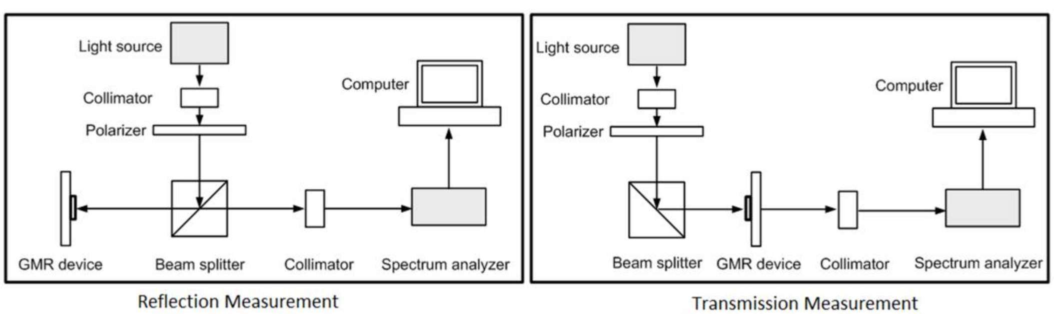

Figure 2-7 Schematic view of the optical measurement setup.

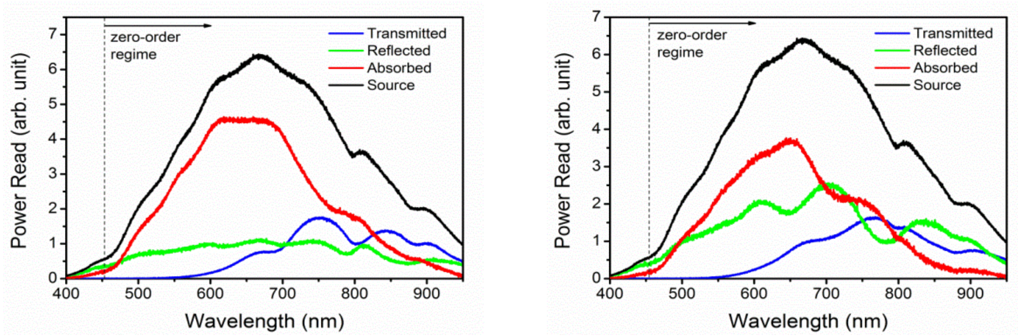

(a) (b)

Figure 2-8 Transmitted, reflected, absorbed, and source spectra of (a) patterned and (b) unpatterned samples.

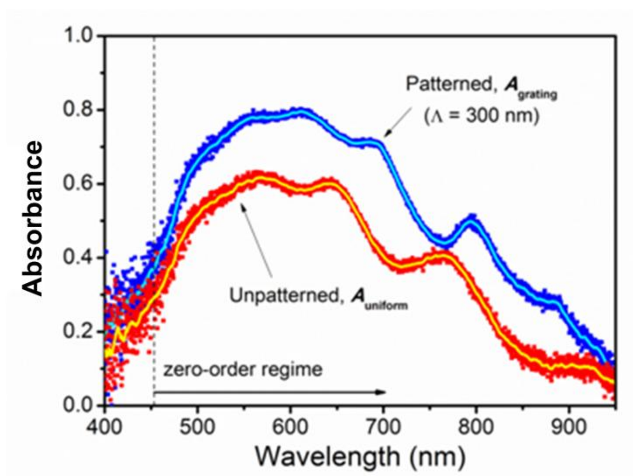

Figure 2-9 Absorbance spectra of patterned and unpatterned samples.

2.5 Conclusions

One-dimensional periodic patterns with a 300 nm period and a 60 nm grating depth are fabricated on 570-nm thick amorphous silicon over glass substrate. Enhanced optical absorption due to the GMR in these films is observed. Integrated absorbance enhancement factor of about 50% is found compared to planar reference thin films for the 400–950-nm wavelength range for the particular device design used. The results motivate deployment of photonic resonance effects to increase efficiency in thin-film solar cells.

Chapter 3

Light Management through GMRs in Thin-Film Photovoltaics

We theoretically explain and experimentally demonstrate light trapping in thin-film solar cells through guided-mode resonance effects. Resonant field enhancement and propagation path elongation leads to enhanced solar absorption. We fabricate nano-patterned solar cells containing embedded 300-nm period, one-dimensional gratings. The grating pattern is fabricated on a glass substrate using laser interference lithography followed by a transparent conducting oxide coating as a top contact. A ~320-nm thick p-i-n hydrogenated amorphous silicon solar cell is deposited over the patterned substrate followed by bottom contact deposition. We measure optical and electrical properties of the resonant solar cells. Compared to a planar reference solar cell, around 35% integrated absorption enhancement is observed over the 450–750-nm wavelength range. This light-management method results in enhanced short-circuit current density of 14.8mA/cm^2, which is a ~40% improvement over planar solar cells. Our experimental demonstration proves the potential of simple and well-designed guided-mode resonant features in thin-film solar cells.

3.1 Introduction

Thin-film solar cell technology offers benefits of low-cost material usage and processing relative to currently dominant crystalline silicon solar cells. In contrast to classic thick, wafer-based silicon cells, the higher absorption coefficients of materials used in thin-film photovoltaics allow for a film thickness of hundreds of nanometers to micrometers. The quality of material can be relatively poor since the charge carriers only travel a distance on the order of the film thickness. However, the low-energy photons suffer from short optical paths that ultimately cause low spectral uptake in the cells near the material’s bandedge [1-3]. Consequently, efficient light-trapping mechanisms are necessary to obtain comparable performance from thin-film solar cells.

By incorporating properly designed photonic nanostructures, incoming sunlight can be trapped inside the absorbing layer while reducing loss caused by reflection and scattering. With a highly concentrated field, a thin absorbing layer sufficiently absorbs most of the solar spectrum. This allows further reduction of the absorbing layer thickness and ensures minimal usage of materials and better collection efficiency for low-quality materials. Numerous studies have been conducted to improve light-capture and collection efficiency of thin absorbing layers. The application of diffractive optics [4-6], random texturing [7,8], antireflective layers [9,10], plasmonics [11-13], photonic crystals [14-16], guided-mode excitation [6,17,18], and three-dimensional structures like nano-wire, nano-dome, and nano-cone solar cells [19-21] shows distinguished improvements in solar absorption. Though each mechanism contributes to the manipulation of optical path lengths inside the films, the most efficient light-harvesting scheme is yet to be convincingly identified. Using numerical simulation tools, it is possible to design micro- or nano-domain photonic structures showing enhanced absorption and photocurrents. However, from a practical point of view, application of such features into solar cells has to be technologically and economically feasible.

Here we report guided-mode resonance (GMR) effects in waveguide-grating structures for enhanced optical absorption. We experimentally demonstrate the application of simple designs of one-dimensional nano-grating patterns into thin-film hydrogenated amorphous silicon (a-Si:H) solar cells. With these particular operative effects, the periodic spatial pattern couples the input sunlight into a collection of waveguide modes associated with thin wave-guiding films that resonate in the cell and concentrate the light in the active layer. Thereby the photon interaction path is elongated within the silicon film, which helps particularly to harvest the low-energy photons. We describe the fabrication processes and present experimental results that comply with our theoretical analysis.

3.2 GMR-Enabled Light Trapping in Thin-Film Photovoltaics

In this study, absorption enhancement in thin-film solar cells by applying the GMR effect is demonstrated. A generic GMR element consists of subwavelength periodic pattern and a waveguide layer over a substrate, as shown in Figure 3-1, with characteristic parameters, period Λ, grating depth d_g, waveguide layer thickness d_{wg}, fill factor F, incident beam I, reflected beam R, and transmitted beam T. The grating layer, which is a phase-matching element, forces incoming light to couple to leaky eigen-modes at resonances. A simple planar structure fails to offer such light confinement. Depending on structural parameters and material properties, GMR elements can exhibit single or multiple resonances. For efficient solar absorption, the GMR structure should support multiple resonances over the broadband solar spectrum. Designing the grating-pattern period to be smaller than the wavelengths in the solar spectrum ($\Lambda < \lambda$) allows the GMR structure to operate as multiple resonant devices. To demonstrate the multi-resonant GMR spectral response, we consider a structure consisting of a a-Si:H grating and a waveguide layer over a glass substrate with Λ = 350 nm, d_g = 50 nm, d_{wg} = 250 nm, and F = 0.5. Hydrogenated a-Si has a complex dispersive refractive index, $N(\lambda) = n(\lambda) + i\kappa(\lambda)$, capable of absorbing light up to the 750-nm wavelength corresponding to bandgap energy of 1.7eV. The numerical value of $N(\lambda)$ provided by Fontcuberta i Morral et al. [22] is given in Figure 3-2.

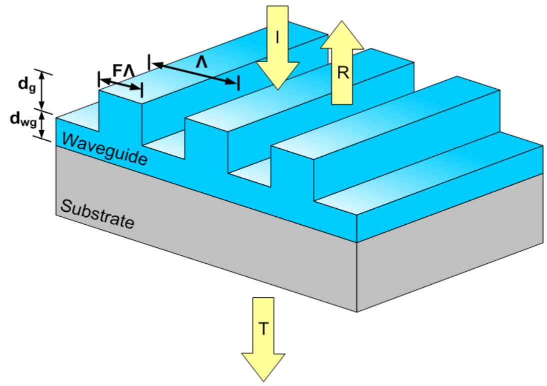

Figure 3-1 Schematic view of generic GMR element.

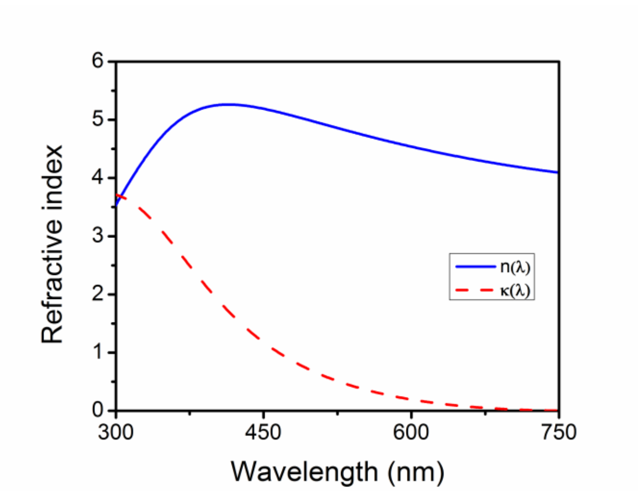

Figure 3-2 Dispersive refractive index of a-Si:H as derived from [22].

Figure 3-3 shows the spectral responses of a multi-resonant GMR structure with three different κ values. Plot 1 indicates lossless a-Si:H with κ = 0, plot 2 indicates a constant κ = 0.05, and plot 3 indicates the original dispersive κ(λ) over the spectrum, while n(λ) remains the same (as in Figure 3-2) for all three plots. The observed resonance peaks originate from input light coupling to leaky-modes across the spectrum. We observe the reduction of reflection and subsequent enhancement of absorption with the increase of the κ value over the spectrum of 450–750-nm wavelengths.

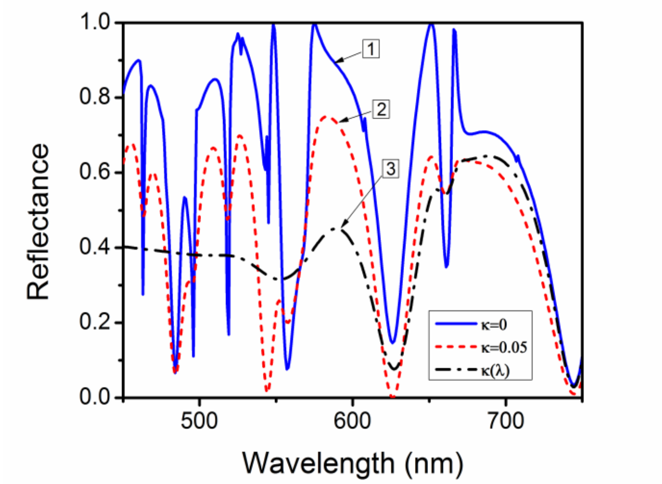

Figure 3-3 GMR spectral response for a waveguide-grating structure with Λ = 350 nm, d_g = 50 nm, d_{wg} = 250 nm, F = 0.5, $n_c = n_L = 1$, and $n_s = 1.5$. Plot 1 represents the GMR effect for lossless material where κ = 0, plot 2 represents the reduced reflectance for lossy material where κ = 0.05, and plot 3 represents reflectance for lossy a-Si:H with the original dispersive κ(λ).

The total electric field patterns for the three different κ values (κ = 0, κ = 0.05, and κ = 0.082) at the 651-nm resonance wavelength are shown in Figure 3-4. The original value of κ at 651 nm is 0.082. Though the field pattern gradually decays with the increase of the κ value, the intensified field profile still prevails which is sufficient to increase the light absorption. Based on the simulation results, we intend to implement the photonic resonant structure into a real p-i-n thin-film a-Si:H solar cell to observe enhanced absorption through intensified field patterns and subsequent increased electrical efficiency. However, fabrication of resonant patterns into the active region of a planar solar cell requires sacrifice of materials and junction interruption, which will cause electrical performance degradation. Instead, we consider a superstrate cell configuration to incorporate the patterns into the active region as schematically shown in Figure 3-5. We fabricate a nano-pattern on a glass substrate, and the pattern is gradually transferred to the silicon region without interrupting the junctions. We consider a thin indium-tin-oxide (ITO) layer in between the glass and silicon as a top contact. To observe the GMR-induced absorbance enhancement exclusively, we conduct the optical characterization before the bottom contact is made.

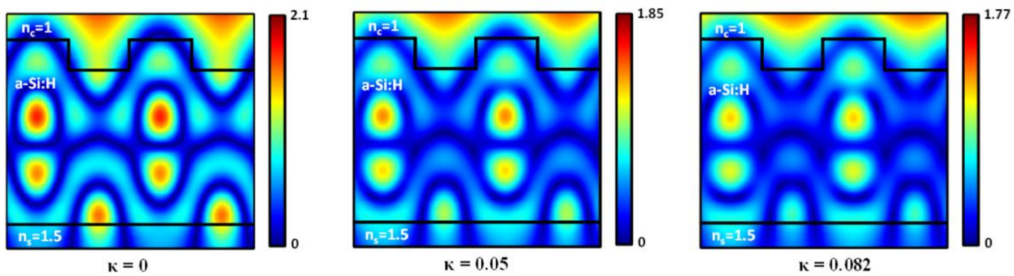

Figure 3-4 Total electric field distribution inside a a-Si:H waveguide-grating structure for three different values of κ (0, 0.05, and 0.082) at λ = 651 nm. The original κ value of a-Si:H at 651 nm is 0.082.

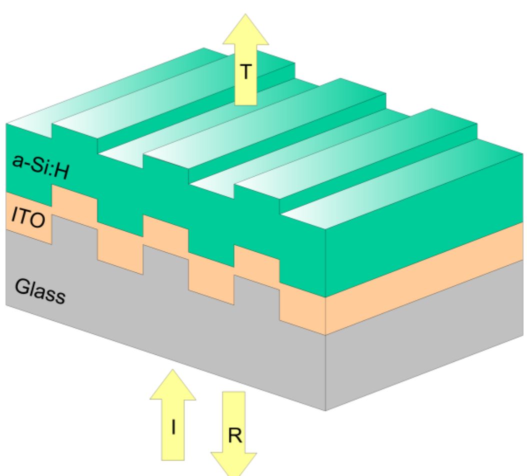

Figure 3-5 Schematic view of a GMR solar cell without bottom contact.

3.3 Fabrication of Nano-Patterned a-Si:H Solar Cells

We fabricate the one-dimensional nano-grating patterns on a glass substrate; Figure 3-6 summarizes the fabrication steps. First, a 1×1 inch^2 glass substrate is cleaned with acetone, isopropanol, and deionized water and dried with blown nitrogen. Then an 80-nm bottom antireflection coating (BARC: DUV30J-6) is spin-coated over the glass substrate at 1200 rpm and baked for 60 seconds on a heating plate adjusted to 205°C. A 350-nm thick photoresist coating (PR: SEPR-701) is spin-coated at 1100 rpm and baked for 90 seconds at 110°C. A one-dimensional grating pattern with a 300-nm period is transferred into the PR by UV laser interferometric lithography using a laser with λ = 266 nm. The purpose of using the BARC layer beneath the PR is to reduce the reflection from the glass substrate and ensure uniform pattern exposure over the PR. After developing the PR, the BARC is removed from the open area of the pattern by reactive ion etching (RIE) using oxygen plasma. The glass substrates are etched using an argon (Ar) and trifluromethane (CHF_3) gas mixture. The remaining PR and BARC is removed by RIE using oxygen plasma. In a systematic experimental process, gratings with 50-, 60-, and 70-nm depths are fabricated on glass substrates. Here, we present the results obtained from solar cells with 60-nm grating depths since the results are similar to those obtained with 50-nm and 70-nm grating depths.

The patterned glass substrates are coated with a 140-nm thick film of ITO by sputtering. From the scanning electron microscope (SEM) images, we confirm that ITO film deposition over the 60-nm deep grating area conforms to the grating structures and serves well as the top contact. The ITO-coated glass substrates are annealed in a rapid thermal annealer (RTA) in a vacuum chamber at 490°C for 15 minutes. The resistivity of the film is 50 ohm/sq. The average transmittance of the annealed ITO thin film is around 90% over the 450–750-nm wavelength range. Figure 3-7 shows the measured transmittance of the annealed ITO film. Using a multi-chambered plasma enhanced chemical vapor deposition (PECVD) system, a complete p-i-n single-junction solar cell with an approximate thickness of 10-nm p-type, 290-nm i-type, and 20-nm n-type a-Si:H is deposited over the ITO pattern. The a-Si:H film is deposited from silane gas (SiH_4). For n-type and p-type doping, phosphine (PH_3) and boron hydride (B_2H_4) gases are added to the gas phase respectively during deposition. Finally, consecutive sputter deposition of 130-nm thick ITO and 300-nm thick aluminum films constitute the bottom contact. Thin-film solar cells on planar glass substrates are also deposited with identical film thicknesses for performance comparison.

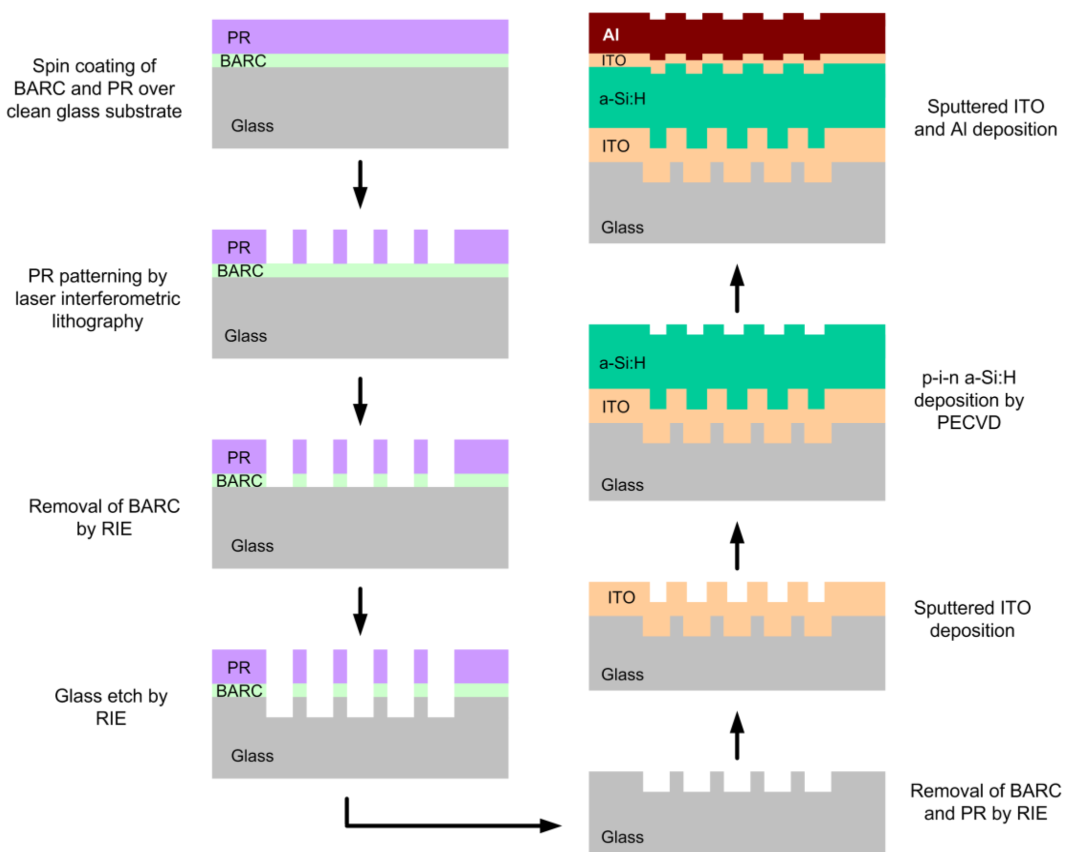

Figure 3-6 Schematic view of nano-patterned solar cell fabrication steps.

The surface image of the ITO-coated oxide grating with a grating depth of 60 nm, taken with an atomic force microscope (AFM), is shown in Figure 3-8. The grating specifications are Λ = 304 nm, d_g = 60 nm, and F = 0.5. Figure 3-9 includes images from an SEM; Figures 3-9 (a–b) show cross-sectional images of the ITO-coated glass pattern, and Figures 3-9 (c) shows the top view. The cross-sectional images of the complete patterned solar cell, including top and bottom contacts, are presented in Figure 3-9 (d–e). Figure 3-9 (f) displays a photograph of the patterned solar cell.

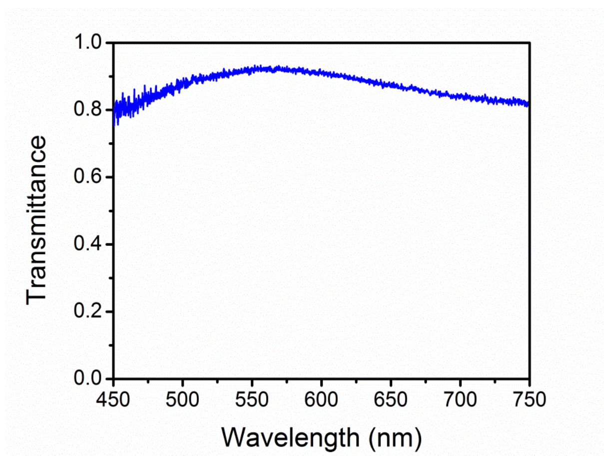

Figure 3-7 Transmittance of an annealed 140-nm thick ITO film deposited on a glass substrate.

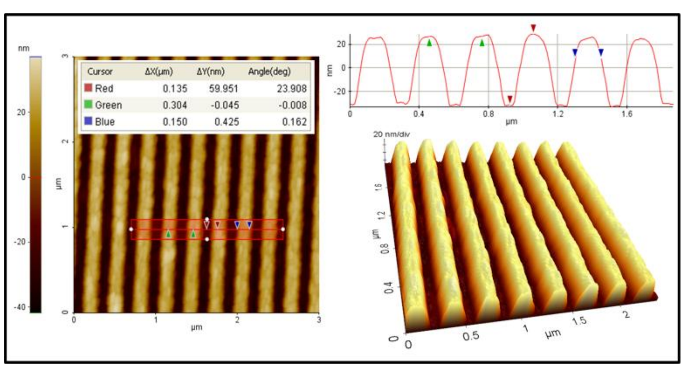

Figure 3-8 AFM surface images of an ITO-coated patterned glass substrate where Λ = 304 nm, d_g = 60 nm, and F = 0.5.

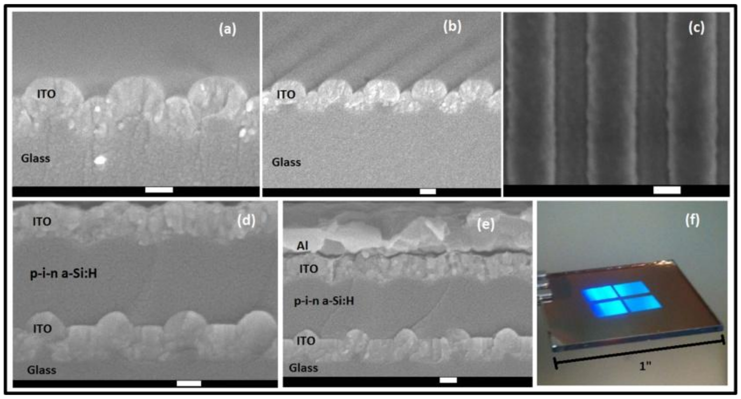

Figure 3-9 (a–b) SEM cross-sectional and (c) top view of ITO-coated glass substrate; (d–e) SEM cross-sectional images of a nano-patterned solar cell; the scale bar is 100 nm in each image; (f) photograph of a nano-patterned solar cell.

3.4 Results and Discussion

3.4.1 Optical Absorbance

Regarding the superstrate structure of the solar cell, Figure 3-5 illustrates that light is shone from the glass side of the structure at normal incidence. We obtain optical absorbance measurements before the bottom contacts are made in order to ascertain GMR-induced absorption enhancement exclusively. The reflected and transmitted light associated with the patterned a-Si:H solar cells is measured with a fiber optic spectrometer. The light source used is a tungsten halogen lamp with a wavelength range of 360–2400 nm. We conduct the same measurements on a corresponding planar solar cell to establish a comparison. Since the grating pattern has a 300-nm period and the refractive index of glass is 1.5, the Rayleigh wavelength of the patterned structure is $\lambda_R = n\Lambda$ = 450 nm, i.e., only the zero-order diffraction prevails beyond the 450-nm wavelength.

The primary reason for selecting a 300-nm period is to operate the solar cells in a zero-order diffraction regime for a substantial portion of the solar spectrum. Since no higher diffraction orders exist beyond the 450-nm wavelength, it suffices as a good approximation to measure the reflectance and transmittance for normally incident light without using an integrating sphere. We measure zero-order reflectance (R_0) and transmittance (T_0) spectra normalized to the source spectrum and the absorbance is obtained as $A = 1- (R_0 + T_0)$ for $\lambda > 450$ nm. The measurement setup is schematically shown in Figure 3-10.

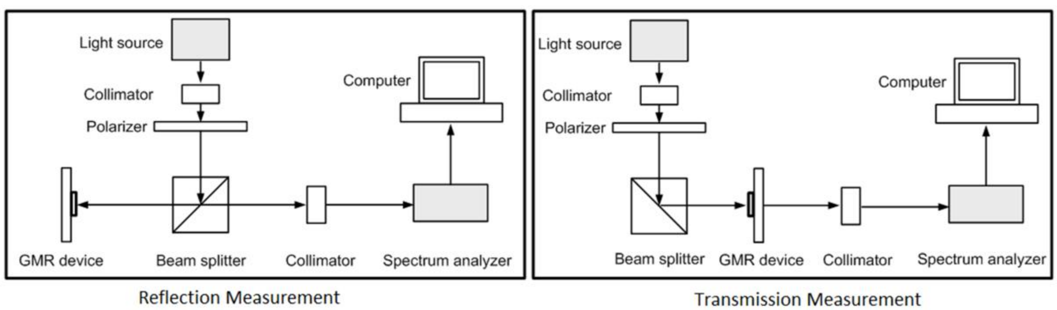

Figure 3-10 Schematic view of the optical measurement setup.

Figure 3-11 shows the comparison of unpolarized absorbance between patterned and planar solar cells. Integrated absorbance enhancement of ~35% is obtained in patterned solar cells with 60 nm deep grating depths over the wavelength range of 450–750 nm. Figure 3-12 shows the unpolarized reflectance comparison between planar and patterned cells. The reflectance is significantly suppressed in patterned solar cells. Designing the period to be smaller than the operating wavelength permits the anti-reflection effect to contribute to the enhanced optical absorbance. Due to this interdependency, it is difficult to differentiate the impact from the GMR effect [6]. However, the absorption coefficient of a-Si:H weakens beyond 550 nm. The propagation distance of the captured light along the weakly absorbing film, i.e., the decay length of the resonant leaky mode, must be much longer than the film thickness to achieve successful absorption in the long wavelength region. Thus, the GMR effect can ensure such optical path elongation through multiple resonances. Figure 3-13 shows the transverse electric (TE) and transverse magnetic (TM) components of the total absorbance of the patterned solar cell, where the electric field vectors in TE and TM polarization are orthogonal and parallel to the plane of incidence, respectively. As described in the previous section, the spectral signature diminishes with a higher extinction coefficient. Therefore, the individual GMR peaks are not visible over the entire wavelength range. In the long wavelength region where the absorption coefficient is low, distinguishable GMR resonances are visible at 716 nm for TM polarization and at 675 nm and 723 nm for TE polarization.

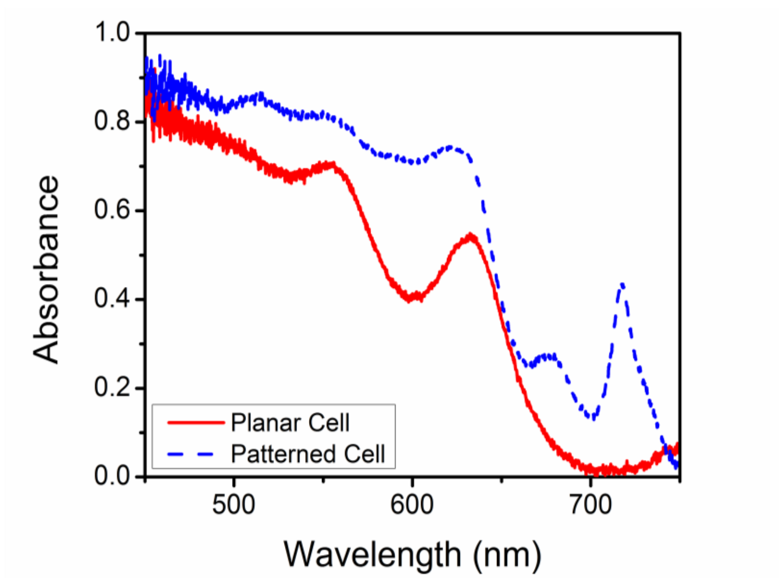

Figure 3-11 Unpolarized absorbance spectra of planar and patterned solar cells at normal incidence of light.

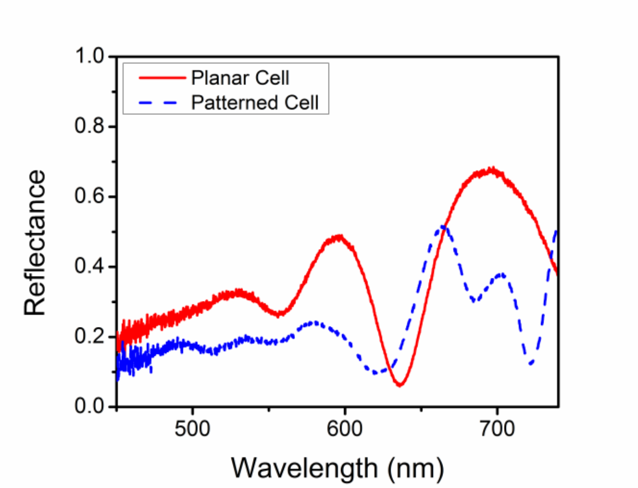

Figure 3-12 Unpolarized reflectance spectra of planar and patterned solar cells at normal incidence of light.

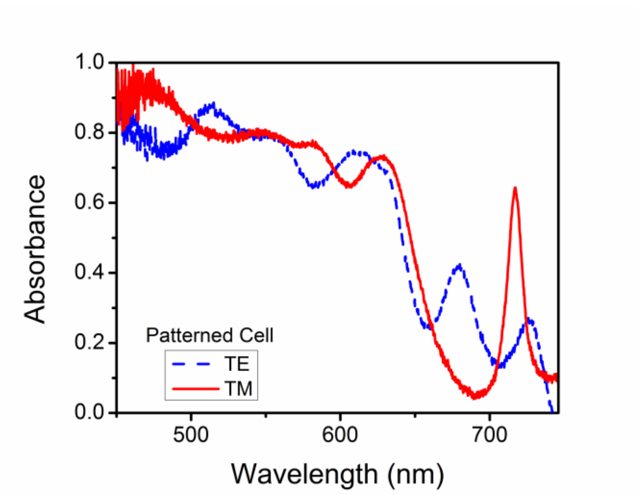

Figure 3-13 TE and TM polarized components of absorbance of a patterned solar cell at normal incidence of light.

The absorbance of the patterned solar cell is theoretically calculated using the RCWA computation method. The simulated and experimental absorbance comparison for a 60-nm deep patterned solar cell is shown in Figure 3-14. There are two possible reasons for the discrepancy. First, the dispersion data of a-Si:H used for simulation is not measured from the fabricated device, rather taken from literature [22]. Second, the fabricated pattern does not completely follow the sharp binary pattern as schematically shown in Figure 3-5. According to simulation, the integrated absorbance enhancement factor is ~32% for patterned solar cell compared to a homogeneous reference, over the 450–750-nm wavelength range.

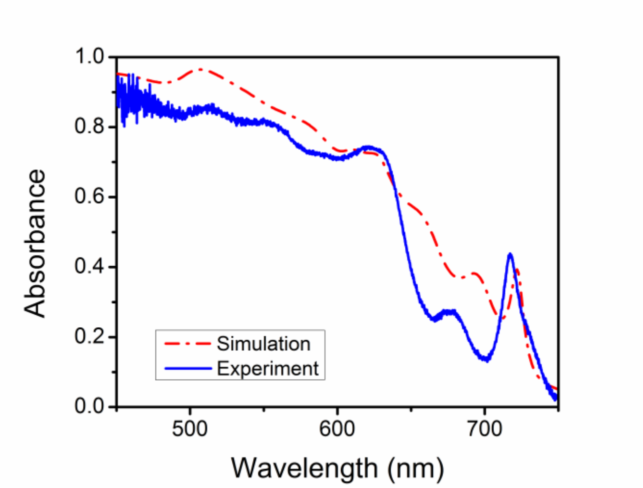

Figure 3-14 Theoretical and experimental comparison of unpolarized absorbance of patterned solar cell with d_g = 60 nm at normal incidence of light.

3.4.2 Electrical Characteristics

Solar cell efficiency measurement is carried out under AM1.5G illumination. The current density (J) versus voltage (V) plots for patterned and planar solar cells are given in Figure 3-15. Open-circuit voltage (V_{oc}), short-circuit current density (J_{sc}), fill factor (FF), and conversion efficiency (η) for the patterned and planar solar cells obtained from J-V plot are summarized in Table 3-1.

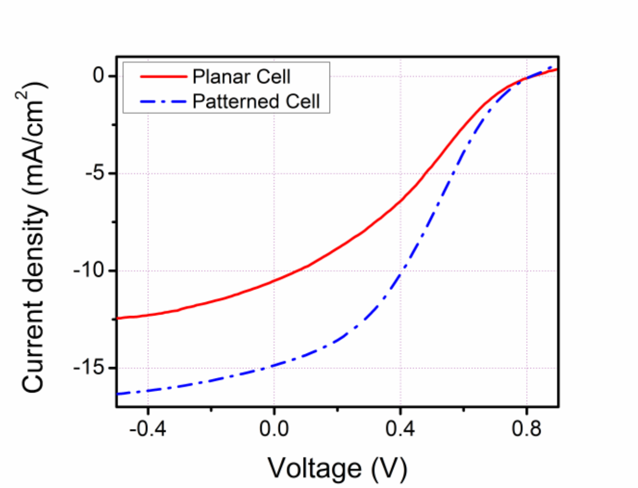

Figure 3-15 Current density/voltage plot of planar and patterned solar cells.

Short-circuit current density improves by ~40% from 10.5 to 14.8mA/cm^2 for patterned solar cells with d_g = 60 nm, compared to the planar cell. Each cell has an effective area of approximately 0.1 cm^2. Open-circuit voltage is 0.82V for both types of solar cells. The power conversion efficiencies of the planar and patterned solar cells are measured as 2.6% and 4.1%, respectively, with ~57% enhancement. The fabricated solar cells exhibit rather low fill factors, which is the main reason for the low conversion efficiencies obtained. Fill factors for the planar and patterned cells are 3 and 3.3, respectively. By enhancing the contact resistivity, a-Si:H material, and p-i-n interface quality, the fill factor and subsequently the efficiency of these solar cells can be improved. The higher optical absorbance obtained through GMR resonances in patterned solar cells compared to the planar reference cell are reflected in the enhanced electrical performance. The experimental results motivate the application of nano-grating patterns in thin-film photovoltaics.

Table 3-1 Electrical Performance Comparison

Parameters	**Planar Cell**	**Patterned Cell**	**Enhancement (%)**
Open-circuit voltage, V_{oc} (V)	0.82	0.82	
Short-circuit current density, J_{sc} (mA/cm^2)	10.5	14.8	~40
Fill factor, FF (%)	3	3.3	
Conversion efficiency, η (%)	2.6	4.1	~57

3.5 Conclusions

We explain light trapping in thin-film solar cells through guided-mode resonances with numerical examples and experimentally implement nano-grating patterns into a-Si:H solar cells with 300-nm periods and 60-nm grating depths. Theoretically simulated GMR-enabled enhanced optical absorption is experimentally observed in fabricated patterned solar cells, which leads to improved electrical performance. For the particular device design used, integrated absorbance enhancement of ~35% over the 450–750-nm wavelength range and short-circuit current density enhancement of ~40% are found in a 60-nm deep nano-grating patterned solar cell compared to an equivalent planar reference cell. GMR phenomena strongly depend on dispersion properties and thickness of the absorbing photovoltaic materials. Enhanced optical absorbance leading to increased conversion efficiency holds the same potential for micro-crystalline and organic thin-film solar cells with optimal structural and material device parameters.

Chapter 4

Fabrication of Thermally Nano-Imprinted Resonant Patterns for Thin-Film Photovolatic Applications

A single-step, low-cost fabrication method to generate resonant nano-grating patterns on poly-methyl-methacrylate (PMMA; plexiglas) substrates using thermal nano-imprint lithography is reported. A guided-mode resonant structure is obtained by subsequent deposition of thin films of transparent conductive oxide and amorphous silicon on the imprinted area. Referenced to equivalent planar structures, around 25% and 45% integrated optical absorbance enhancement is observed over the 450-nm to 900-nm wavelength range in one- and two-dimensional patterned samples, respectively. The fabricated elements provided have 300-nm periods. Thermally imprinted thermoplastic substrates hold potential for low-cost fabrication of nano-patterned thin-film solar cells for efficient light management.

4.1 Introduction

In order to achieve efficient light absorption in thin-film solar cells, photonic nano-patterns are of great interest. Two basic approaches are considered to increase light interaction in solar media through nano- and micro-structures. One approach is to use an antireflective layer with a gradually changing refractive index profile to enhance optical transmission [1]. The other approach is to trap light inside the cell. Common light trapping schemes include use of front and/or back random texturing to scatter light as well as deployment of metallic or dielectric gratings to induce plasmon or quasi-guided modes, respectively, to confine light in the waveguide region [2, 3]. Along with one-dimensional (1D) and two-dimensional (2D) patterns, three-dimensional (3D) dome-, cone-, or rodshaped structures are reported with enhanced conversion efficiencies [4–6]. The resonant photonic patterns are applicable to silicon solar cells and are promising for third-generation organic photovoltaics. However, additional fabrication steps of nano- or micro-domain features using conventional photolithography and subsequent etching of respective materials adds to production cost. Thus, the main challenge remains to improve low-cost and large-area fabrication techniques of such patterns. To overcome this issue, nano-imprint lithography (NIL) is a promising alternative.

The basic concept of NIL is to transfer a pattern from a master (or a mold) to various substrates under pressure [7–9]. The desired nano-patterns are normally fabricated first as master templates using photolithography or e-beam lithography and wet or dry etching. Various materials such as silicon, quartz, or metals can be used as masters. The substrate may have a spin-coated polymer resist layer that is subsequently cured by ultra-violet (UV) or infrared (IR) light, or it can be a thermoplastic substrate softened by a thermal source. Thermally activated NIL process is also known as hot embossing lithography. The master may or may not need a release agent depending on the type of substrate material used. Laser-assisted direct imprinting on inorganic films using excimer lasers has also been reported [10].

NIL is applied in vast topical areas including organic and inorganic thin-film transistors, light emitting diodes (LEDs) and organic LEDs, and organic and thin-film solar cells [7]. For thin-film solar cell applications in particular, NIL technique is mostly applied to fabricate antireflection layers. One- or double-sided imprinted films are fabricated separately and later attached on top of the solar cells [11–14]. For light trapping, imprinted randomly textured substrates are fabricated to scatter light in thin films of solar cells [15–17]. In contrast to scattering, light trapping through coupling quasi-guided or leaky modes into the waveguide region of solar cells requires resonant structures with precise shape and periodicity on the order of the operating wavelength. Few studies have been done on periodic nano-pattern fabrication using soft-NIL and nanomoulding [18, 19], and simple and easy fabrication techniques based on these concepts still needs to be conquered.

We have reported on enhanced solar uptake in thin-film hydrogenated amorphous silicon solar cells through guided-mode resonance (GMR) effects [20]. Here we complement our research by presenting a simple, easy, and faster fabrication approach of the nano-patterns with periods smaller than the operating wavelength using thermal nano-imprinting lithography. The technique involves fewer processing steps than soft-NIL and nanomoulding, circumvents solution process spin coating or UV-source curing, ensures high repeatability and a large printing area, and uses low-cost materials. These characteristics make the method suitable as an integrated step in production of thin-film photovoltaic devices.

4.2 Experiments

4.2.1 Master Fabrication

The master grating is made of quartz, and Figure 4-1 schematically shows the fabrication steps. A 1x1-inch^2 quartz substrate is cleaned with acetone, isopropanol, and deionized water; the substrate is then dried with blown nitrogen. An 80-nm-thick bottom antireflection coating (BARC) is spin-coated at 1200 rpm and baked for 60 seconds on a heating plate adjusted to 205°C. A 300-nm-thick photoresist (PR) layer is subsequently spin-coated at 1100 rpm and baked for 90 seconds on a heating plate at 110°C. Both 1D and 2D grating patterns with a period of 300 nm are transferred to the PR using UV laser interferometric lithography. 2D grating patterns require double exposure with 90° sample rotation between exposures. After developing, the BARC layer in the PR windows is removed by oxygen plasma. Quartz is etched down to 66 nm for the 1D and 75 nm for the 2D grating using an argon (Ar) and trifluromethane (CHF_3) gas mixture in a reactive-ion etch (RIE) chamber. The remaining PR and BARC are removed using oxygen plasma.

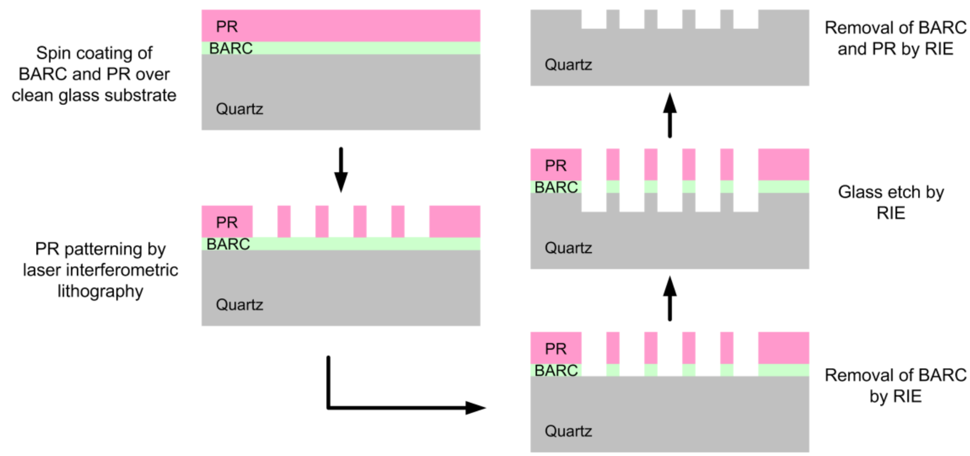

Figure 4-1 Schematic view of nano-patterned master fabrication steps on quartz substrate.

4.2.2 Imprinted Plexiglas Fabrication

Plexiglas (polymethyl methacrylate, PMMA) is a thermoplastic material transparent to visible light. It has a luminous transmittance of 92%. Figure 4-2 shows the measured transmittance over the 400-nm to 700-nm wavelength range. The refractive index is 1.49 at the 589.3-nm wavelength [21], and the glass transition temperature (T_g) is 105°C. Plexiglas with higher T_g, up to 165°C, is also available. A ~1.5-mm thick plexiglas sheet is used for the experiments.

A schematic view of the pattern transfer setup is shown in Figure 4-3. A quartz master is placed on a heating plate, and the plexiglas substrate sits on top of it. A load in the form of a metal chunk is applied from the top side to create a pressure of 1.57 bar

(22.8 psi). The pressure is applied before the heating plate is turned on. When the temperature rises above T_g, the plexiglas behaves as a viscous liquid and under pressure allows the quartz grating to penetrate the substrate. The temperature of the heating is adjusted so that the temperature of the master, as measured by a thermocouple, is maintained at 160°C. After 60 minutes at 160°C, the heating plate is turned off and cooled down to 60°C after which the pressure is released. The imprinted plexiglas is ejected without any adhesion or damage to the master. We notice that the fabricated grating area on the master and the imprinted area on plexiglas is the same, 5x5mm^2. With a larger fabricated master grating area and uniform application of pressure over plexiglas, larger imprinted grating areas can be obtained.

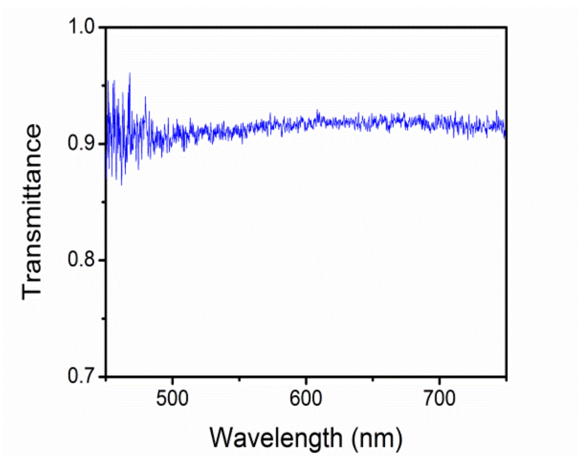

Figure 4-2 Measured transmittance of plexiglas.

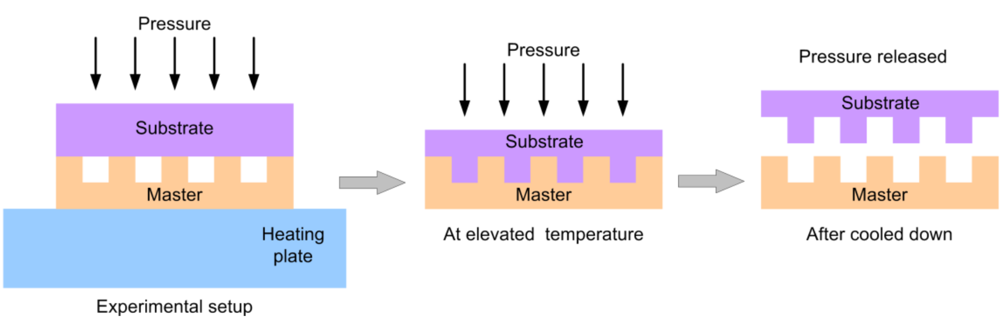

Figure 4-3 Schematic summarizing thermal nano-imprinting.

The grating geometry of a GMR element is defined by the period (Λ), fill factor (F), and grating depth (d_g); Figure 4-4 shows a schematic picture. Atomic force microscope (AFM) and scanning electron microscope (SEM) images are taken to characterize the profile dimensions of the fabricated nano-patterns. The AFM images of 1D and 2D master grating profiles are shown in Figures 4-5 and 4-6, respectively. Figures 4-7 and 4-8 present the AFM images of respective imprinted plexiglas. Table 4-1 gives the profile dimensions obtained from the AFM/SEM images. The period of both master and imprinted gratings is 300 nm as measured with AFM. The 1D master grating depth is 66 nm whereas the imprinted grating depth is 65 nm as measured with AFM. The 2D master grating and the imprinted grating depths are 75 nm as measured with AFM; the fill factors are 0.45 and 0.55, respectively. The dimensions obtained from the AFM images closely match the SEM images shown in Figure 4-9. Figure 4-9 (a) and 4-9 (d) show the SEM images of quartz masters with a 1D and 2D grating, respectively, and 4-9 (b) and 4-9 (e) show the corresponding imprinted plexiglas. These topological SEM images show that the fill factor is approximately the same in the copy as in the master. Small cracks are observed on the imprinted plexiglas, which are due to the gold films deposited for improved visibility of the SEM images.

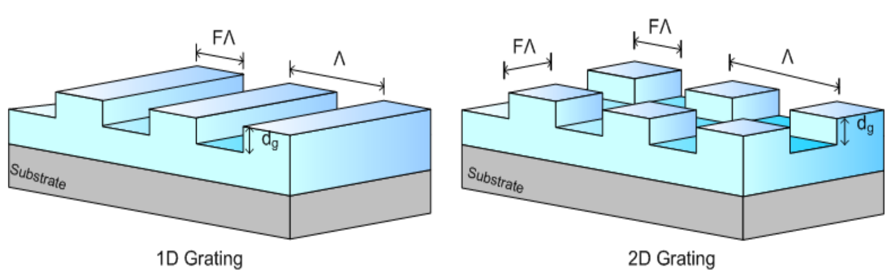

Figure 4-4 Schematic view of grating geometry showing period (Λ), fill factor (F), and grating depth (d_g).

Table 4-1 Characteristic Numbers of Grating Profiles Obtained from AFM and SEM Images

Parameters	**Values**			
	Master (1D)	**Imprinted Plexiglas (1D)**	**Master (2D)**	**Imprinted Plexiglas (2D)**
Period (Λ)	300 nm	300 nm	300 nm	300 nm
Grating Depth (d_g)	66 nm	65 nm	75 nm	75 nm
Fill Factor (F)	0.5	0.5	0.45	0.55

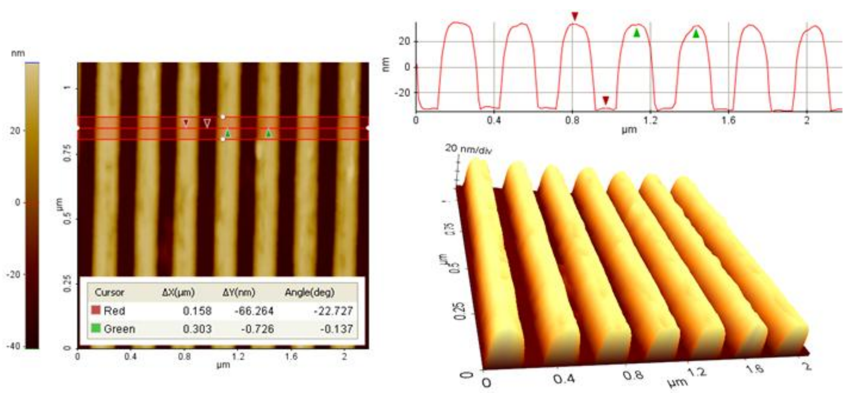

Figure 4-5 AFM images of the quartz master 1D grating.

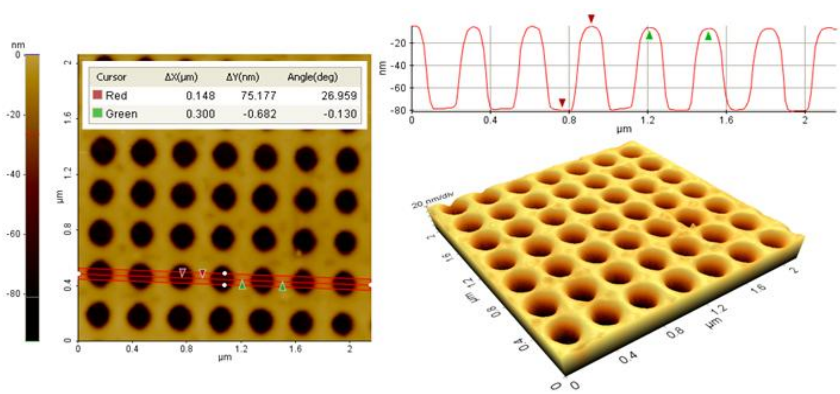

Figure 4-6 AFM images of the quartz master 2D grating.

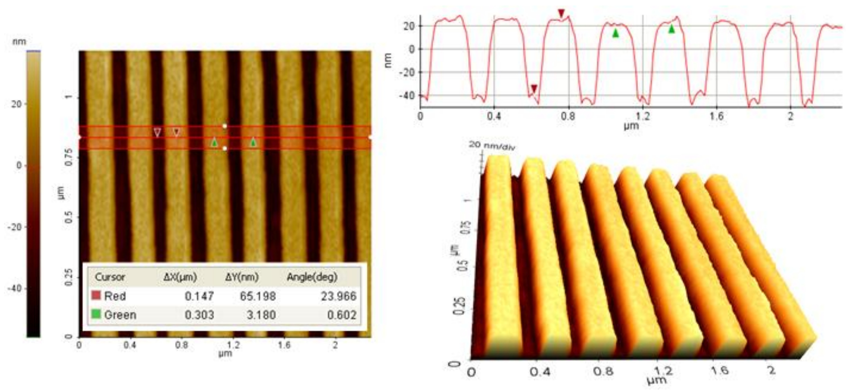

Figure 4-7 AFM images of the imprinted plexiglas 1D grating.

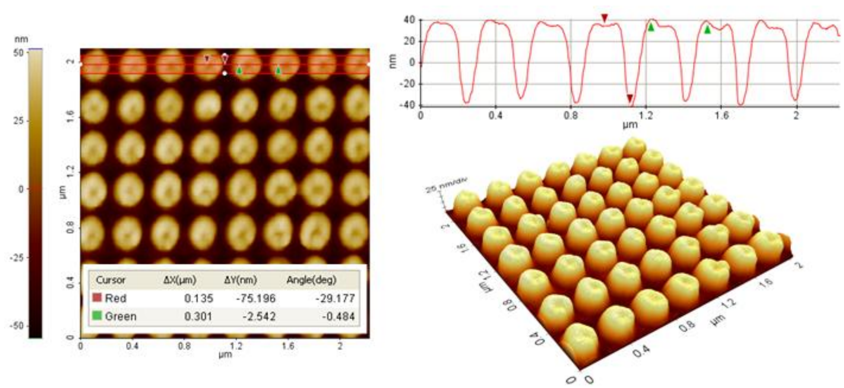

Figure 4-8 AFM images of the imprinted plexiglas 2D grating.

4.2.3 ITO and a-Si Film Deposition on Plexiglas Grating

To observe the optical absorbance enhancements enabled via the imprinted grating structures, 80-nm-thick indium-tin-oxide (ITO) layers and 200-nm-thick amorphous silicon (a-Si) layers are deposited via sputtering over the imprinted plexiglas. As a reference sample, identical films are deposited on top of a planar plexiglas substrate. In principle, the presence of the ITO film has little effect on the optical enhancement but is applied to mimic a thin-film solar cell in order to demonstrate the potential of the imprint method for solar cell fabrication. Light is shone from the plexiglas side to realize a superstrate configuration of a solar cell with ITO serving as the front transparent conducting oxide. Figure 4-10 gives a schematic view of the structure with incident (I), reflected (R), and transmitted (T) beams. Figures 4-11 and 4-12 visualize the AFM surface image of ITO-coated patterned plexiglas. The grating depths after ITO coating remain similar, 67 nm for the 1D grating and 76 nm for the 2D grating. The SEM images of the ITO-coated nano-patterns are included in Figure 4-9. Shallow grating patterns with grating depths of approximately 22 nm for the 1D grating and 35 nm for the 2D grating are transferred to the top surface of the a-Si layer after a 200-nm-thick a-Si deposition over the ITO pattern as shown in Figure 4-13.

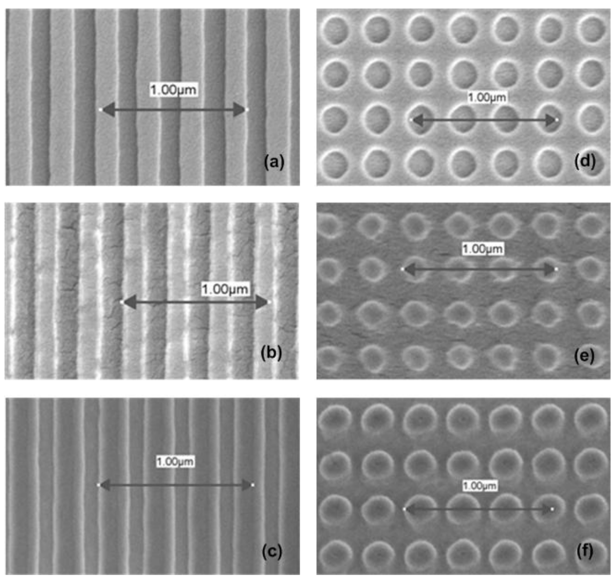

Figure 4-9 SEM images of the (a) 1D quartz master grating, (b) 1D imprinted plexiglas grating, (c) ITO-coated 1D imprinted plexiglas grating, (d) 2D quartz master grating, (e) 2D imprinted plexiglas grating, and the (f) ITO-coated 2D imprinted plexiglas grating.

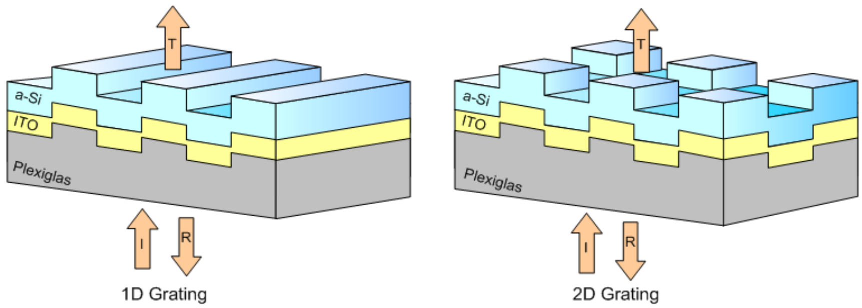

Figure 4-10 Schematic view of fabricated nano-patterned a-Si film; arrows indicate the directions of the incident, reflected, and transmitted beams.

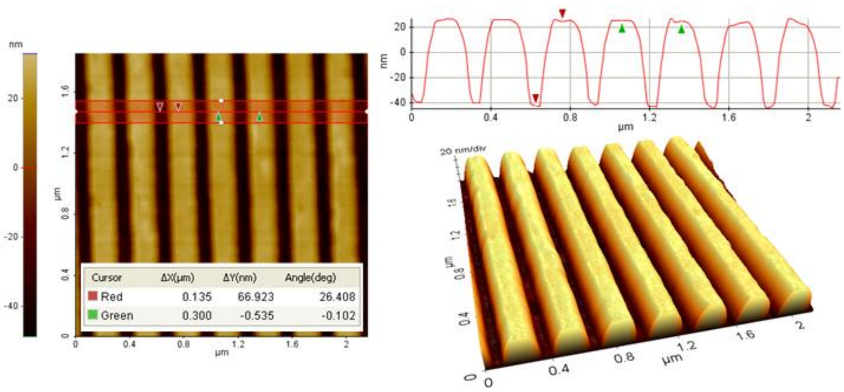

Figure 4-11. AFM surface images of the ITO-coated patterned plexiglas substrate 1D grating.

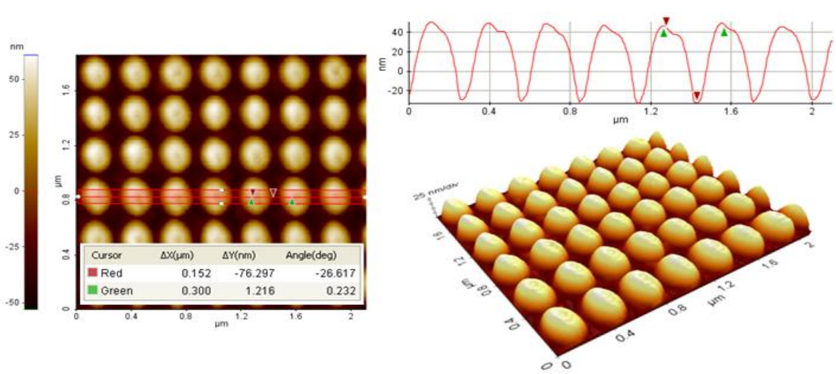

Figure 4-12 AFM surface images of the ITO-coated patterned plexiglas substrate 2D grating.

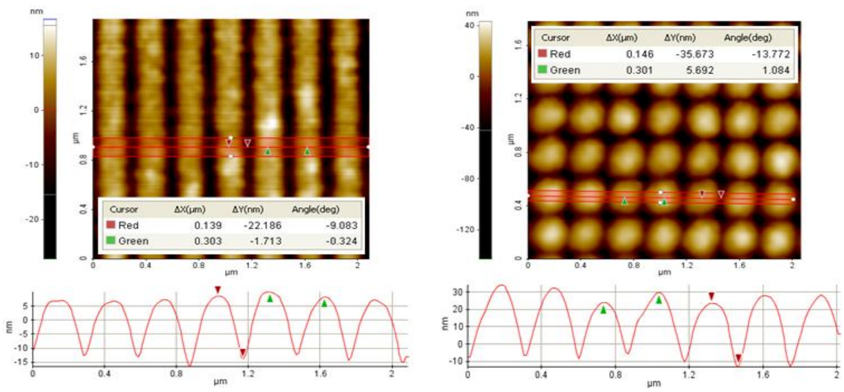

(a) (b)

Figure 4-13 AFM surface images of a-Si over an ITO layer. (a) 1D and (b) 2D grating.

4.3 Results and Discussion

A fiber optic spectrometer is used to measure the transmitted and reflected light from the fabricated devices shown in Figure 4-13. Light is shone normally from the plexiglas side as Figure 4-10 depicts. Taking the refractive index of plexiglas as 1.49 and the period of the grating as 300 nm, the Rayleigh wavelength of the patterned structure is $\lambda_R = n\Lambda \approx 450$ nm. Hence, only zero-order diffraction prevails beyond 450 nm. Reflectance (R_0) and transmittance (T_0) spectra normalized to the source spectrum are measured, and the absorbance is obtained as $A = 1\text{-}R_0\text{-}T_0$. Figure 4-14 shows the comparison of unpolarized absorbance between patterned and unpatterned reference samples at normal incidence. Integrated optical absorbance enhancement of about 25% for 1D and 45% for 2D nano-patterns is observed over the 450-nm to 900-nm wavelength range. Figure 4-15 gives the polarization dependent absorbance for a 1D grating pattern.

We recall that even in these thin patterned films, a large number of resonant leaky modes fundamentally exists across the spectral region of interest in this work. The modes can be visualized by artificially setting the imaginary part of the complex refractive index to zero as exemplified in Ref. [22]. In a real material, the modes at shorter wavelengths experience large absorption and the spectrum appears smooth without discernible resonance peaks. As the absorption falls with increasing wavelength as in normal material dispersion, the modal signatures become more distinct. Thus in our experiments, besides broadband monotonic absorption at shorter wavelengths, distinguishable resonance-based absorption peaks are observed at longer wavelengths as particularly evident at 762 nm for transverse electric (TE) and at 792 nm for transverse magnetic (TM) polarizations. At first, this result may appear curious to an experimentalist assuming that these are the signatures of the fundamental TE and TM modes as the TE modal resonance should appear at the longer wavelength. Here, the TE mode is in fact not the fundamental mode but rather the TE_1 mode. To illustrate this, we compute the total electric and magnetic field distributions at resonance using rigorous coupled-wave analysis [23]. Figure 4-16 (a) shows that a TE_1-like mode profile belongs to the resonant peak at 762 nm. Figure 4-16 (b) demonstrates the TM_0 mode profile associated with the peak at 792 nm.

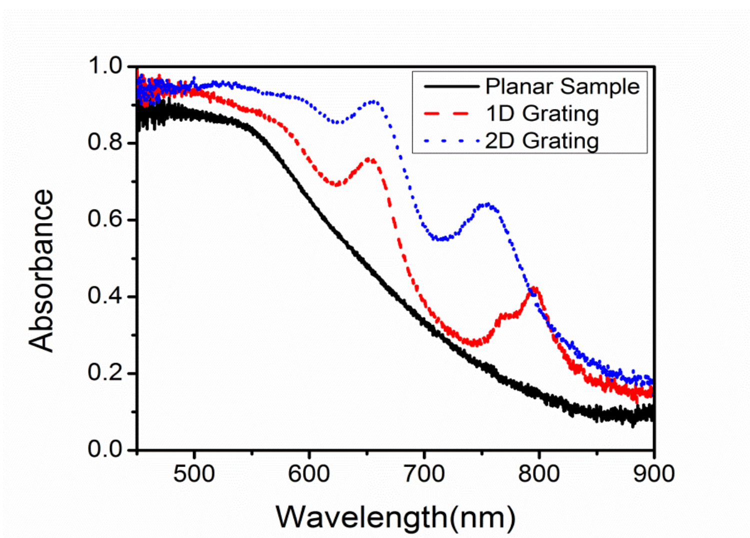

Figure 4-14. Unpolarized absorbance spectra of planar reference and imprinted patterned samples at normal incidence of light.

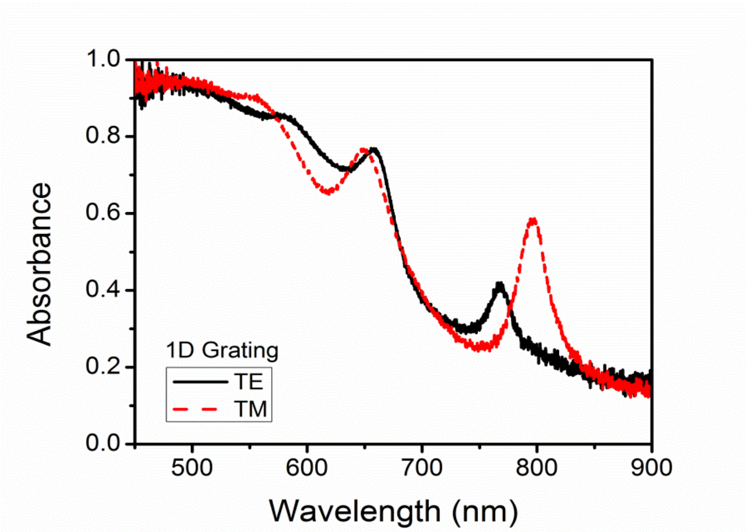

Figure 4-15 TE (electric field vector normal to the plane of incidence) and TM (electric field vector parallel to the plane of incidence) polarized components of absorbance of the 1D grating patterned sample at normal incidence of light.

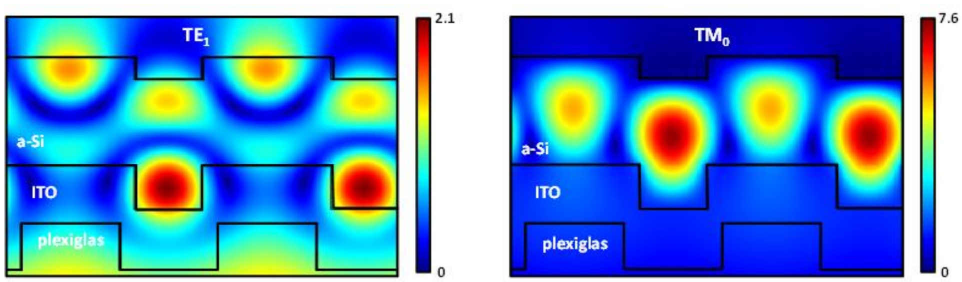

(a) (b)

Figure 4-16 Total (a) electric field distribution for TE_1 mode excitation at the 762-nm wavelength (b) magnetic field distribution for TM_0 mode excitation at the 792-nm wavelength, observed in the absorbance spectra of the 1D grating sample shown in Figure 4-15.

Conversely, the 2D grating pattern exhibits a polarization-independent response as shown in Figure 4-17. In general, for both 1D and 2D patterned devices, the absorbance response and enhancement will vary widely for different photovoltaic absorbing materials and embodiments. Indeed, the occurrence and density of GMRs depends on the complex dielectric constant and its dispersion properties as well as on the thickness, fill factor, and grating modulation strength of the absorbing waveguide-grating layer system.

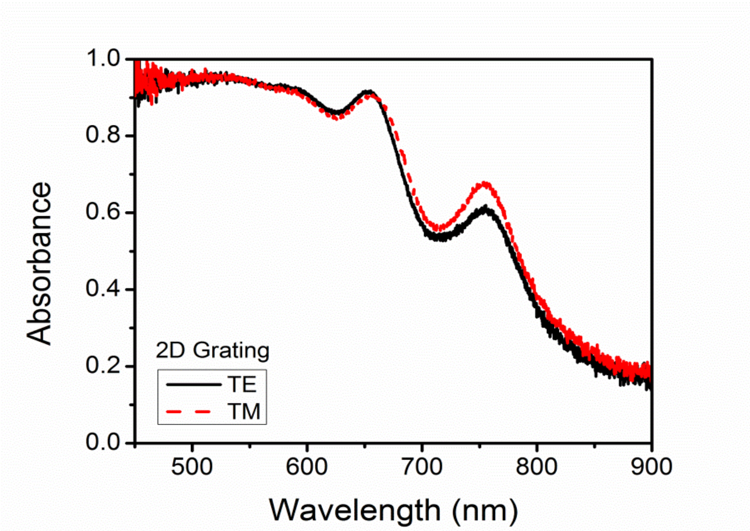

Figure 4-17 TE and TM polarized components of absorbance of the 2D grating patterned sample at normal incidence of light.

As visualized by the surface images in Figure 4-13, the sharpness of the 1D and 2D patterns decreases on account of the ITO deposition and still further upon a-Si film deposition. This does not substantially affect the optical enhancement obtained since the pattern period and dimensional regularity persist.

4.4 Conclusions

A low-cost approach to nano-pattern fabrication of resonant thin-film solar cells for efficient light trapping is proposed and experimentally demonstrated. The process includes a single step to fabricate the pattern on a substrate, which eliminates the need for photolithography and RIE steps. Imprinted 1D and 2D elements containing nano-patterns with a 300-nm period on thermoplastic substrates are designed and fabricated. The spectral variation of optical absorbance in thin a-Si films is measured, and it shows integrated absorption enhancement of ~25% for 1D and ~45% for 2D grating patterns across the 450-nm to 900-nm wavelength range, referenced to planar samples, for the particular device embodiments studied. Future research work may extend this methodology to real thin-film p-i-n solar cell fabrication over patterned imprinted substrates. Single-step fabrication methods facilitate production by enabling roll-to-roll printing of substrates for thin-film solar cells including organic photovoltaics. The thermal nano-imprint fabrication technique described in this study is not limited in shape or dimension of the pattern profile. Once a master grating is fabricated with a desired photonic structure and reasonable aspect ratios, concomitant patterns can be replicated with high repeatability and a long master lifetime.

Chapter 5

Design and Fabrication of GMR Broadband Reflectors

We present the design and fabrication of guided-mode resonant broadband reflectors operating in transverse electric (TE) polarization. The structure consists of a subwavelength one-dimensional grating with a two-part period and a nanometric homogeneous layer of amorphous silicon on a quartz substrate. A representative reflector exhibits 99% reflectance over a 380-nm spectral range spanning 1440–1820 nm. The fabrication involves thin-film deposition, interferometric lithography, and reactive ion etching. Experimental reflectance greater than 90% is achieved over a ~360-nm bandwidth. The spectral bandwidths demonstrated exceed formerly reported results for two-part periodic resonators working in TE polarization.

5.1 Introduction

Wideband reflectors based on photonic resonances are important because of their diverse design possibilities and integration compatibility for application in couplers, resonant cavity-enhanced photodetectors, and lasers [1-4]. These reflectors exhibit less material losses than metal mirrors and avoid multilayer depositions traditionally required for dielectric stack mirrors. These reflectors reveal guided- or leaky-mode resonances (GMRs or LMRs) and are most effectively fashioned as subwavelength waveguide grating structures. With proper parametric design, engineering the spectral, polarization, and phase attributes of GMR reflectors is achievable to match numerous applications.

Transverse electric (TE) and transverse magnetic (TM) resonant reflectors using subwavelength two-part or multipart periodic grating structures have been studied in the past [5-11]. Reviewing briefly, for TM polarization, Mateus et al. demonstrated a two-part device with a ~500-nm bandwidth [5] whereas Ding et al. reported four-part structures with a ~600-nm bandwidth [6]. For TE polarization, Ding et al. presented a four-part reflector with a ~600-nm bandwidth [6], and Wu et al. reported a ~630-nm bandwidth for a similar element [7]. Additionally, Wu et al. reported the fabrication results of a six-part TE device with reflectivity $R > 97\%$ over a 240-nm bandwidth [8], and Lee et al. fabricated a two-part TE structure with $R > 90\%$ over a ~130-nm bandwidth [9]. We addressed the physical basis for GMR wideband reflectors in [10] and investigated the effects of added sublayers on the reflection response and bandwidth in [11]. In summary, TE-polarized wideband resonant reflectors with multipart periods have been achieved whereas the simpler two-part devices that are much easier to fabricate show markedly narrower bandwidths in the published literature. In this contribution, we aim at ameliorating this condition by designing and fabricating new resonant reflectors in this class.

Accordingly, in this study, we present theoretical and experimental spectra pertaining to TE-polarized reflectors with two-part periods operating in the optical communication band. The structures consist of one-dimensional (1D) silicon grating patterns with integral nanometric silicon sublayers deposited on silica substrates. We find that the homogeneous layer plays a crucial role in extending the bandwidth. A similar resonant structure was recently reported and operated as a Rayleigh reflector [12]. This study elaborates the design approach with systematic parametric variations to tune the bandwidth. The fabrication and characterization processes are described in detail.

5.2 Device Structure and Design

The generic GMR element consists of a subwavelength periodic grating and a homogeneous layer on a substrate. Figure 5-1 shows the schematic view of a device model with the characteristic design parameters being period (Λ), fill factor (F), grating depth (d_g), and homogeneous layer thickness (d_h). The refractive indices of cover, device, and substrate are denoted as n_c, n, and n_s, respectively.

Figure 5-2 shows the reflectance and transmittance spectra of a wideband reflector for normally incident TE-polarized light. We use rigorous coupled-wave analysis (RCWA) for the computations [13]. The design parameters are Λ = 960 nm, F = 0.5, d_g = 320 nm, and d_h = 55 nm. The structure's Rayleigh wavelength is $\lambda_R = n_s\Lambda$ = 1440 nm, where n_s = 1.5 is the refractive index of the quartz substrate; the reflectance in Figure 5-2(a) drops sharply at this wavelength. Beyond λ = 1440 nm, only zero-order diffraction prevails. The figure shows R_0 > 99% over a ~380-nm bandwidth in the 1440-nm to 1820-nm wavelength range. Two transmission dips exist inside the reflection band at 1465 nm and 1771 nm as depicted on a logarithmic scale in Figure 5-2(b); each dip corresponds to a GMR. Since 100% reflection is associated with GMRs, the interaction between these two side-by-side resonances yields wideband reflection.

Varying the device parameters such as homogeneous layer thickness, grating depth, and fill factor changes the number and loci of resonances, which ultimately tunes the bandwidth. The effect of changing each of the parameters is described in successive sections. Among these variable parameters, tuning the homogeneous layer thickness is essential for making the reflector wideband in nature as reduced bandwidths are seen in its absence.

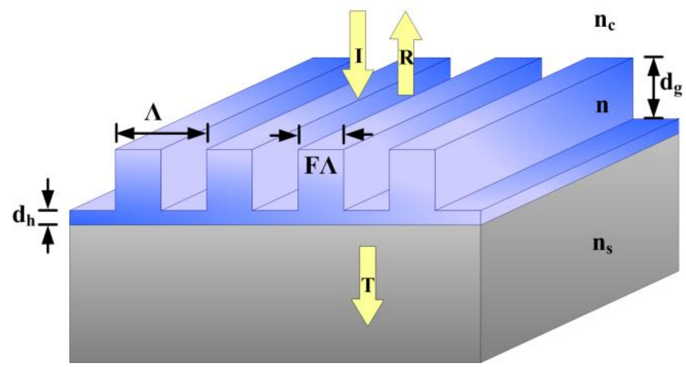

Figure 5-1 Wideband reflector model denoting the period Λ, fill factor F, grating thicknesses d_g, homogeneous layer thickness d_h, and refractive indices of cover n_c, silicon n, and substrate n_s. The incident (I), reflected (R), and transmitted (T) light waves are indicated. The TE-polarized incident light's electric field vector is orthogonal to the plane of incidence and along the grating ridges in this case. We set $n_c = 1$, n = 3.56, and substrate $n_s = 1.5$ in this study.

5.2.1 Effect of Homogeneous Layer Thickness

Figure 5-3 shows a zero-order reflectance (R_0) map plotted against wavelength and homogeneous layer thickness with the parameters set as Λ = 960 nm, F = 0.5, and d_g = 320 nm. With an increasing value of d_h, the two GMRs separate correspondingly. Interaction between closely located resonances ensures high reflectivity but lowered bandwidth, whereas distantly located resonances yield a wider bandwidth with lowered reflectivity in the middle. For example, when d_h = 45 nm, the two GMRs are located close together at 1491 nm and 1640 nm, resulting in a reflector with $R_0 > 99\%$ over the 1440- to 1729-nm (289 nm) wavelength range as shown in Figure 5-4(a); R_0 is shown on a linear scale, and T_0 is shown on a logarithmic scale. When d_h = 75 nm, the GMRs locate farther apart at 1456 nm and 1940 nm, and the reflectance value drops to 96% at λ = 1700 nm.

In this case, R_0 > 95% in the 1440- to 1988–nm wavelength range, providing a 548-nm bandwidth as shown in Figure 5-4(b). As evident in Figure 5-3, the reflector's bandwidth narrows when $d_h \rightarrow 0$. Hence, determining a proper value of the homogeneous layer thickness is essential to obtain a wideband TE reflector. When the thickness of the homogeneous layer exceeds ~100 nm, the reflectivity drops significantly because the GMRs are located too far apart to interact strongly as depicted in Figure 5-3.

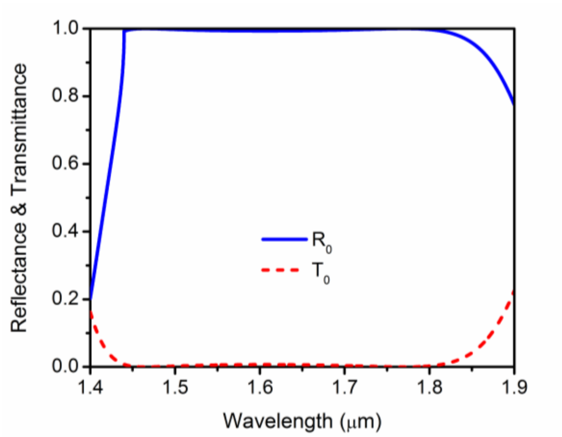

(a)

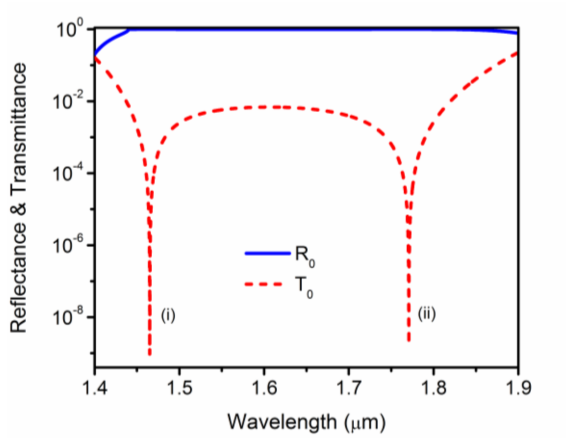

(b)

Figure 5-2 Zero-order reflectance and transmittance spectra; (a) linear and (b) logarithmic plots for normal incidence of TE-polarized light. Device parameters are Λ = 960 nm, F = 0.5, d_g = 320 nm, and d_h = 55 nm.

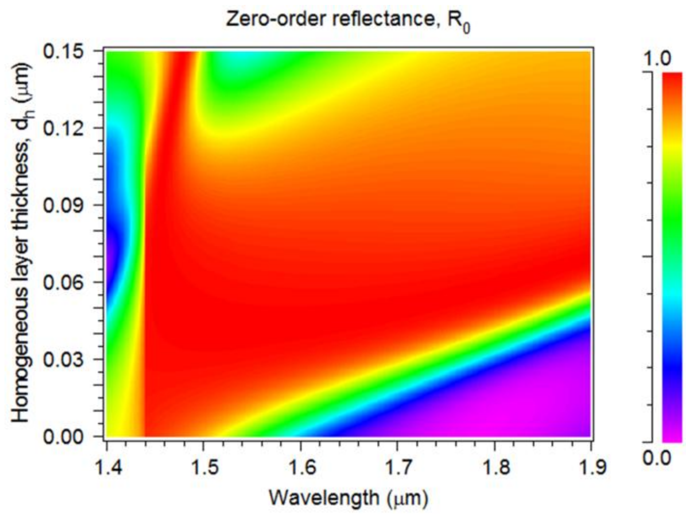

Figure 5-3 Map of zero-order reflectance in wavelength and homogeneous layer thickness. The reflectance is quantified according to the scale bar on the right.

5.2.2 Effect of Grating Thickness

Figure 5-5 displays a zero-order reflectance map showing wavelength and grating thickness with the other parameters set as Λ = 960 nm, F = 0.5, and d_h = 55 nm. The reflector's bandwidth is determined by the grating depth as the spectral positioning of the GMRs varies with d_g. In this example with an increasing value of d_g, the two GMRs approach each other and the bandwidth of the reflector gradually decreases. When d_g = 290 nm, the two transmission dips are located farther apart and the reflectivity drops to 96% at λ = 1700 nm as depicted in Figure 5-6(a). Nevertheless, R_0 > 95% is achieved over a ~450-nm bandwidth. Thus, a broadband reflector prevails with a lowered value of maximum reflectivity. When d_g = 350 nm, R_0 > 99% over a 340-nm bandwidth as shown in Figure 5-6(b). In this particular example, when the grating thickness exceeds 400 nm, the flat band shifts to longer wavelengths and narrows as illustrated in Figure 5-5. Charting R_0 across a wider thickness range would bring in new regions of flat-band reflection as demonstrated in [10,11]; in this study, we emphasize the minimal device for expedient fabrication.

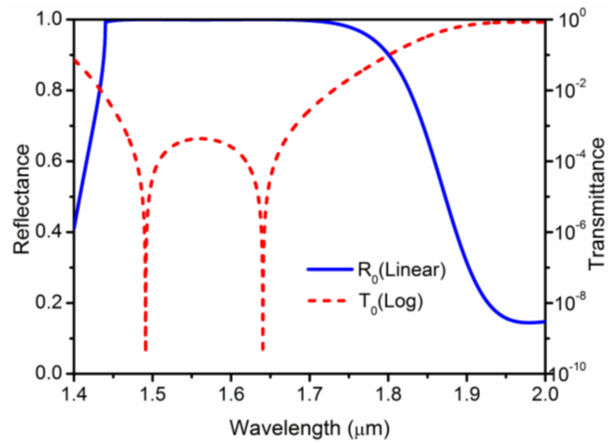

(a)

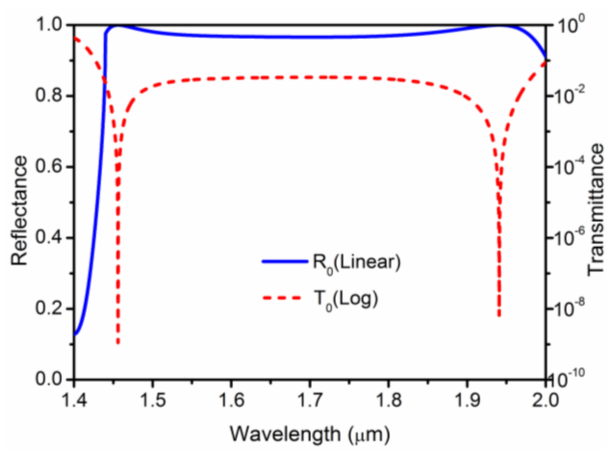

(b)

Figure 5-4 Zero-order reflectance (linear scale) and transmittance (log scale) spectra for (a) d_h = 45 nm and (b) d_h = 75 nm with Λ = 960 nm, F = 0.5, and d_g = 320 nm.

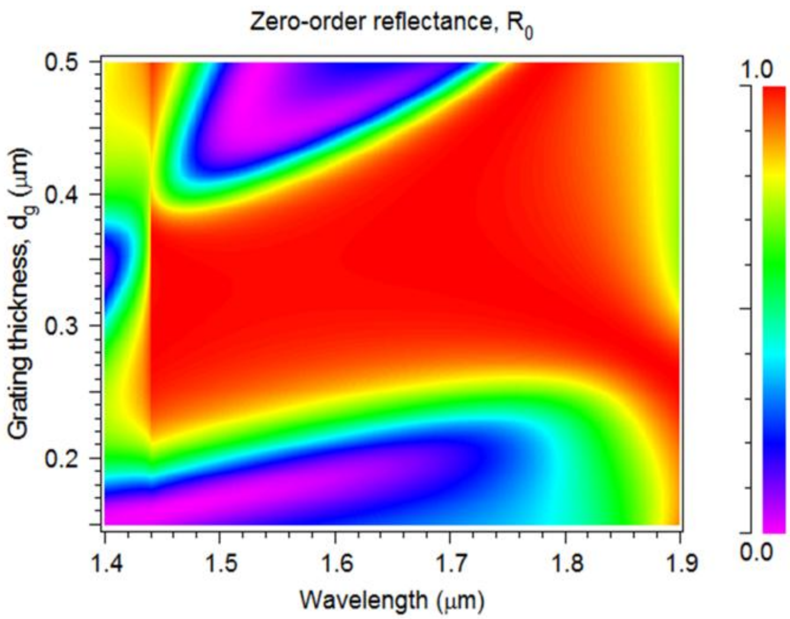

Figure 5-5 Map of zero-order reflectance in wavelength and grating thickness. The reflectance is quantified according to the scale bar on the right.

5.2.3 Effect of Fill Factor

Figure 5-7 shows R_0 plotted against wavelength and fill factor for Λ = 960 nm, d_g = 55 nm, and d_g = 320 nm. A single GMR exists in the device up to F = 0.48, beyond which two GMRs prevail. When F = 0.45, the only transmission dip occurs at λ = 1683 nm, yielding R_0 > 99% across a 316–nm bandwidth as shown in Figure 5-8(a). When F = 0.55, the reflector produces R_0 > 95% over a 438-nm bandwidth as depicted in Figure 5-8(b).

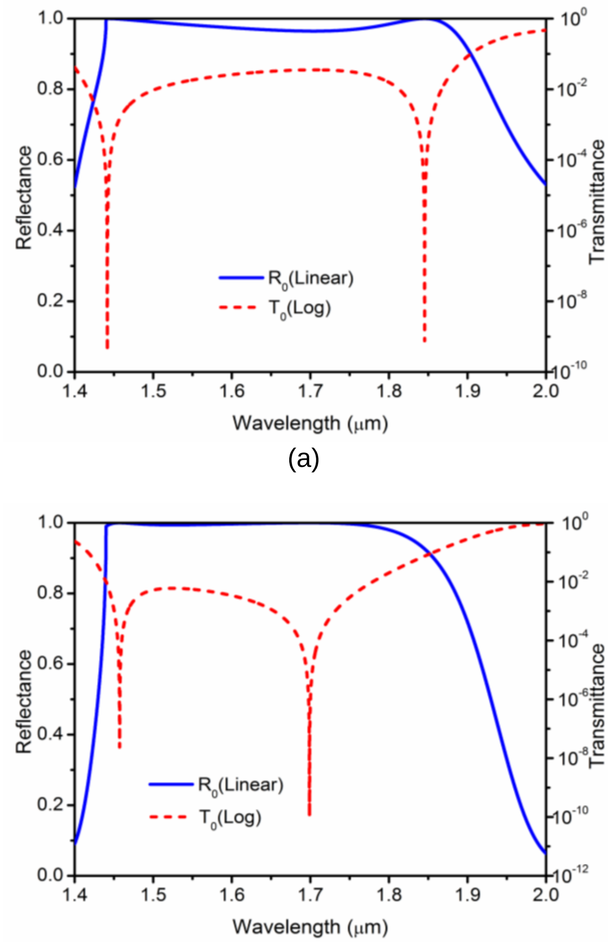

(a)

(b)

Figure 5-6 Zero-order reflectance (linear scale) and transmittance (log scale) spectra for

(a) d_g = 290 nm and (b) d_g = 350 nm with Λ = 960 nm, F = 0.5, and d_h = 55 nm.

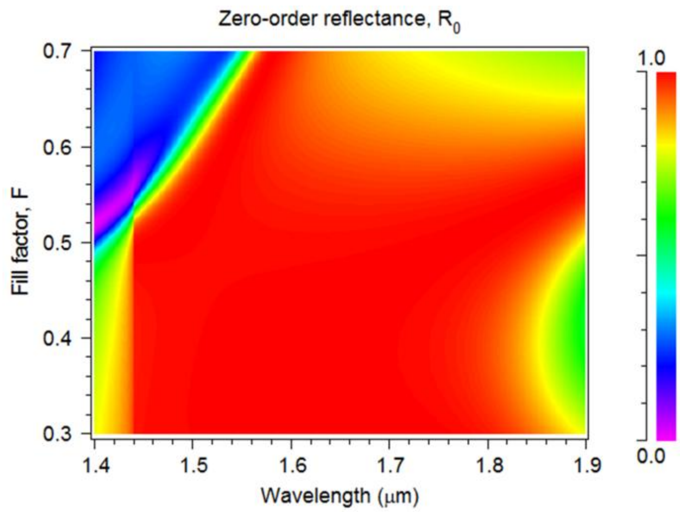

Figure 5-7 Map of zero-order reflectance in wavelength and fill factor. The reflectance is quantified according to the scale bar on the right.

5.3 Fabrication of GMR Broadband Reflectors

A schematic of the step-by-step fabrication process is shown in Figure 5-9. The fabrication commences with deposition of amorphous silicon (a-Si) on a clean quartz substrate by sputtering. The film thickness is 375 nm as verified with ellipsometry. A 400-nm-thick photoresist (PR) layer is then spin-coated on the a-Si film. A 1D grating pattern with a 960-nm period is recorded on the PR by laser interferometric lithography using a deep ultraviolet (UV) laser (λ = 266 nm). The exposed patterned area is 5×5 mm^2. After developing the PR, reactive ion etching (RIE) using a gas mixture of trifluromethane (CHF_3) and sulfur hexafluoride (SF_6) is used to etch down the silicon to 320 nm leaving a ~55-nm sublayer. The residual PR is removed by RIE with oxygen plasma.

The device is characterized using an atomic force microscope (AFM) and a scanning electron microscope (SEM). Figure 5-10 shows the AFM image where Λ = 958 nm, F = 0.5, and d_g = 320 nm, which are close to the design parameters. The top-view and cross-sectional SEM images of a similar device in Figure 5-11 show acceptable fabrication uniformity as well as the etch profile and a nanometric homogeneous layer adjacent to the glass substrate. In Figure 5-11, we use a device with the same a-Si film thickness and period as the measured device to save the measured wideband reflector reported in this study from the gold-coat and cross-sectional cut needed to take SEM images.

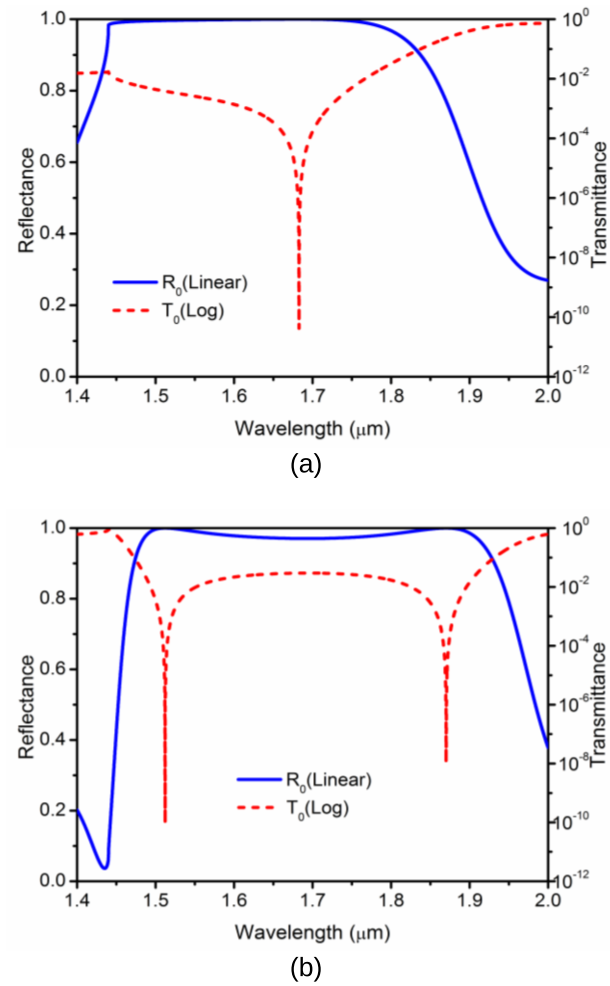

Figure 5-8 Zero-order reflectance (linear scale) and transmittance (log scale) spectra for (a) F = 0.45 and (b) F = 0.55 with Λ = 960 nm, d_g = 320 nm, and d_h = 55 nm.

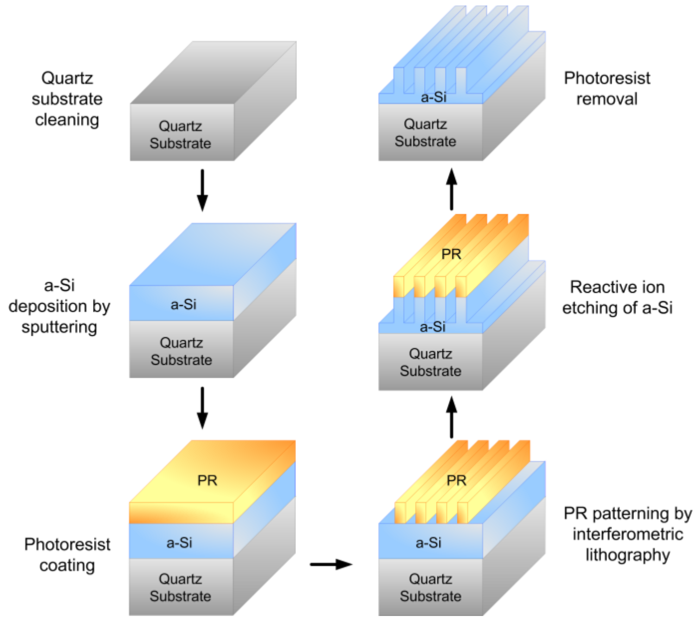

Figure 5-9 A schematic of the GMR reflector fabrication process.

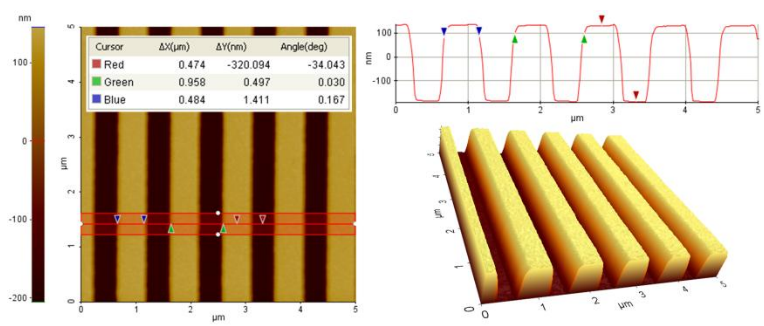

Figure 5-10 AFM image and profile of the fabricated a-Si grating. The parameters are Λ = 958 nm, F = 0.5, and d_g = 320 nm.

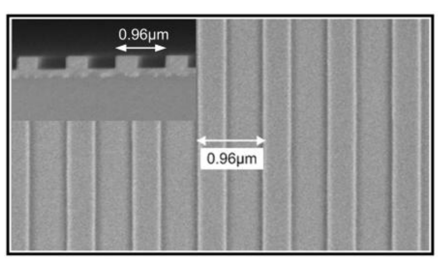

Figure 5-11 SEM top-view and cross-sectional images of a similar a-Si grating pattern on a glass substrate.

5.4 Results and Discussion

The spectral response is measured using a super-continuum source and an optical spectrum analyzer for a wavelength range of 1400–1900 nm. A polarizer is used to choose the TE polarization of the input light. After measuring the reflected light from the device, it is normalized with respect to light intensity from a reference gold mirror. The schematic diagram of the measurement setup at normal incidence of light is given in Figure 5-12.

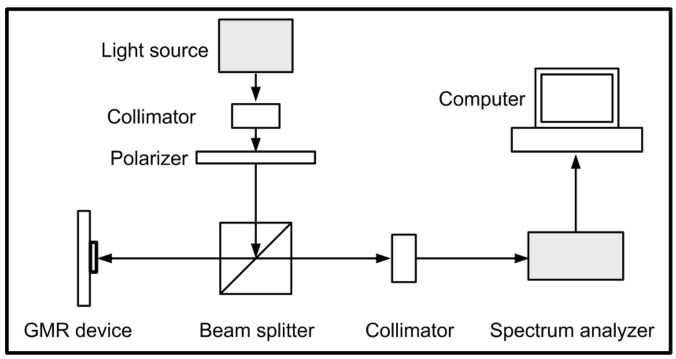

Figure 5-12 Schematic diagram of the optical measurement setup.

Figure 5-13 gives the theoretical and experimental spectra of the fabricated resonant reflector. The parameters obtained from AFM and SEM images are used for simulation. The theoretical bandwidth is 380 nm with $R_0 > 99\%$, which is 255 nm larger than the result reported by Shokooh-Saremi et al. in [11] for a two-part grating structure for TE polarization. Measured performance of the fabricated device shows $R_0 > 90\%$ over ~360 nm ranging from 1478 nm to 1838 nm. The reduced efficiency obtained in experiments compared to the simulated results can be attributed to the combined effect of scattering from surface roughness, absorption associated with the a-Si material, and differences in the experimental device profiles relative to the simulation model. A piecewise linear fitting is used to eliminate ripples in the measured data. The experimental bandwidth is 230 nm higher than the result published by Lee et al. in [9].

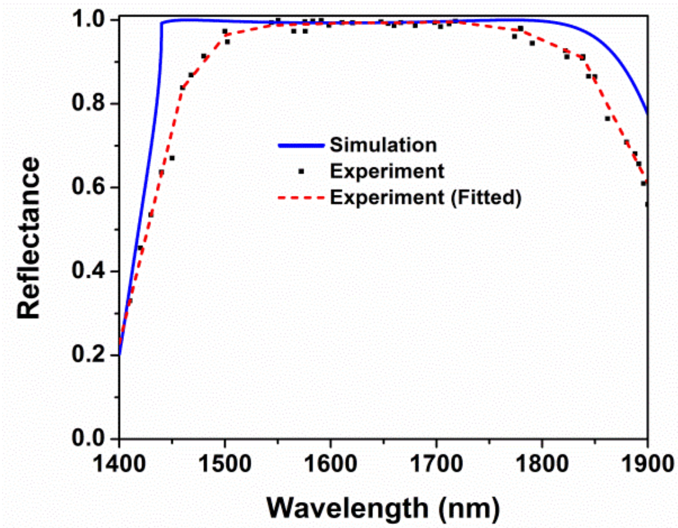

Figure 5-13 Calculated and experimental spectra associated with a resonant reflector with TE-polarized light at normal incidence. The parameters used for computation are Λ = 960 nm, F = 0.5, d_g = 320 nm, d_h = 55 nm, n = 3.56, n_c = 1, and n_s = 1.5.

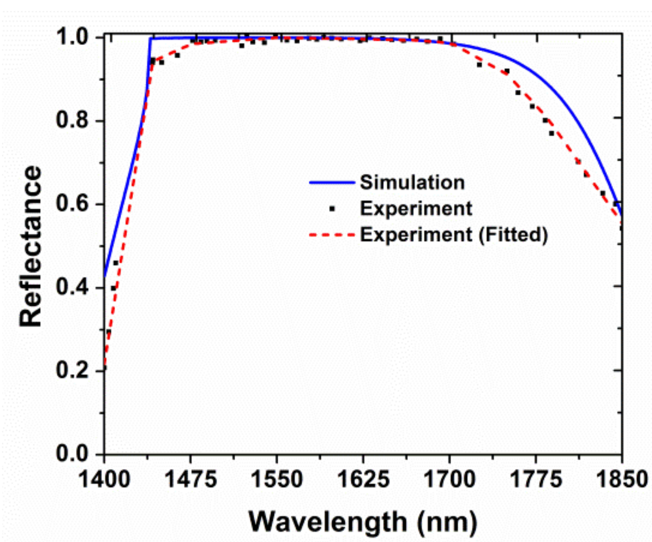

Figure 5-14 Calculated and experimental spectra for a reflector for TE-polarized light at normal incidence. The parameters used for computation are Λ = 960 nm, F = 0.49, d_g = 330 nm, d_h = 45 nm, n = 3.56, n_c = 1, and n_s = 1.5.

Figure 5-14 shows theoretical and experimental spectra of a similar wideband GMR reflector with different parametric values, namely Λ = 960 nm, d_g = 330 nm, d_h = 45 nm and F = 0.49. Since this device has a larger grating depth and smaller homogeneous layer thickness than the former design, it exhibits a lower computed bandwidth of 260 nm with R_0 > 99%. It has an experimental R_0 > 90% for a bandwidth of 315 nm ranging from 1437 to 1752 nm. The theoretical and experimental data for both devices are summarized in Table 5-1.

Table 5-1 Comparison of Theoretical and Experimental Results

R_0	**Bandwidth (nm) Device 1 (d_g = 320 nm, d_h = 55 nm, and F = 0.5)**		**Bandwidth (nm) Device 2 (d_g = 330 nm, d_h = 45 nm, and F = 0.49)**	
	Theoretical	**Experimental**	**Theoretical**	**Experimental**
R_0 > 99%	~380	~220	~260	~225
R_0 > 90%	~430	~360	~340	~315

5.5 Conclusions

We design and fabricate wideband GMR reflectors operating in TE polarization for normally incident light in the telecommunication spectral region. The device consists of a simple 1D grating along with a nanometric homogeneous layer of a-Si on a quartz substrate. The bandwidth and the efficiency of reflectors in this class can be tuned by properly selecting the values of grating depth, fill factor, and homogeneous layer thickness as demonstrated herein via extensive numerical simulations. Experimentally, a ~360-nm bandwidth wide reflector with R > 90% over the 1478- to 1838-nm wavelength range is achieved. The bandwidths demonstrated for these two-part devices in TE polarization exceed those previously reported in the literature.

Chapter 6

Research on Rayleigh Reflectors

We theoretically explain and experimentally verify the concept of flat-top resonant Rayleigh reflectors, a potential application of the Rayleigh anomaly. A rapid energy exchange between a reflected zero-order wave and a substrate wave across a small angular interval is foundational to this effect; it is investigated in some detail with numerical computations. We fabricate a Rayleigh reflector consisting of a subwavelength periodic pattern in an amorphous silicon film on a glass substrate leaving a nanometric homogenous layer in between these. A precipitous change in the zero-order reflectance at the Rayleigh angle is observed experimentally and shown to enable angularly delimited spectra in agreement with theoretical predictions.

6.1 Introduction

In some specific circumstances, spatially modulated periodic lattices exhibit abrupt transitions in diffraction efficiency sometimes referred to as optical anomalies. Thus, externally observable optical intensities change rapidly relative to wavelength or angle of incidence of the input wave. Wood first observed these natural phenomena associated with diffraction gratings [1]. There are two principal types of anomalous effects [2]. The first one is the Rayleigh type and second is the resonance type anomaly. The Rayleigh anomaly (RA), which is the classical Wood's anomaly, is due to the redistribution of energy when a diffracted wave from a periodic surface changes from propagating to evanescent or vice versa, upon variation of input wavelength or incident angle [3]. The resonance type is due to the incident wave being coupled to possible guided modes supported by the waveguide-grating structure [4]. The modal resonance anomaly is known as the guided-mode resonance (GMR) effect [5, 6].

Whereas the RA has been known for over a century, very few studies have been done concerning useful applications of such behavior. Collecting the main results, the Rayleigh anomaly was found to interact with surface plasmon polariton resonances in palladium subwavelength hole arrays and produce interesting, potentially useful, effects [7]. The effect of the Rayleigh anomaly operating in conjunction with a Fabry-Perot resonance was reported and found to increase extraordinary optical transmission efficiency of a metallic grating [8]. In dielectric, lossless, materials, of chief interest in the present work, the combined effect GMR and RA has been shown to produce extraordinary spectral signatures [9, 10]. Amin et al. reported transmission filters based on the GMR effect cooperating with RA [9]. They showed that the onset of higher diffraction orders at the Rayleigh anomaly sharpens the GMR transmission peak. Magnusson introduced the concept of Rayleigh reflectors in which sharp angular spectra can be stimulated [10]. He showed that a theoretical 100% reflectance of the device abruptly drops to zero at the Rayleigh angle when a swift energy exchange occurs between the zero-order reflected wave and the first order substrate propagating wave. Some possible applications of such reflectors are also mentioned in [10]. The diversification of the concept is yet to be explored and thus an extensive understanding of the phenomena is necessary. In summary, the GMR-RA effect holds the potential to stimulate a new research area in which photonic devices with interesting and useful attributes can be invented.

Here we report new Rayleigh reflectors operating in the telecommunications spectral region. Their operating principles are investigated and interpreted through numerical simulations. By way of a fabricated prototype, the rapid energy exchange at the Rayleigh angle is experimentally observed and thereby the Rayleigh reflector concept is verified.

6.2 Device Structure and Design

A schematic model of a Rayleigh reflector is shown in Figure 6-1. The characteristic parameters are denoted as period Λ, fill factor F, grating depth d_g, and homogeneous layer thickness d_h. The refractive indices of the substrate, silicon and cover region are set to n_s=1.5, n=3.56 and n_c=1, respectively. The structure has period sufficiently smaller than the operating wavelength and thus exhibits only zero-order transmitted (T_0) and reflected (R_0) propagating waves at normal incidence. The device parameters are chosen such that with varying incident angle, there exist only ±1 diffraction orders in the substrate.

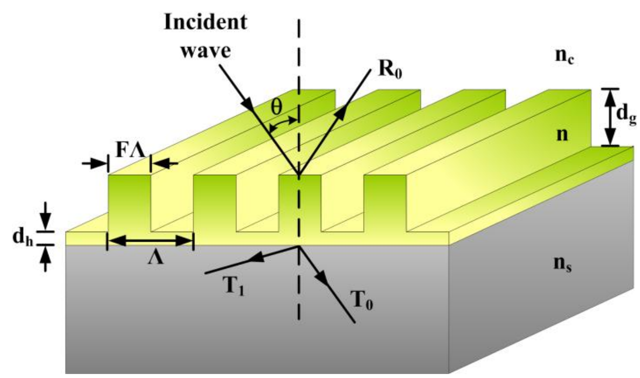

Figure 6-1 Schematic diagram of the Rayleigh reflector denoting period (Λ), fill factor (F), thicknesses (d) of layers, refractive indices (n) of different regions, incident angle (θ) along with reflected (R_0) and transmitted (T_0, T_1) waves.

Using the design parameters Λ = 1028 nm, F = 0.43, d_g = 319 nm and d_h = 60 nm, a reflectance map plotted against wavelength and incident angle is depicted in Figure 6-2. The incident light is transverse-electric (TE) polarized where the electric field vector is orthogonal to the plane of incidence. We use rigorous coupled-wave analysis (RCWA) for these computations [11]. From the figure, it is evident that for a very narrow window of wavelengths, the reflectance value drops from unity to almost zero at a specific incident angle. The transfer of diffracted power takes place from the zero-order reflectance (R_0) to a first-order propagating wave (T_1) beyond the Rayleigh angle which is given as,

$$\sin\theta_R = -n_s + \lambda / \Lambda \tag{6.1}$$

This Rayleigh reflector effect for this particular device design occurs at 1621 nm wavelength. The angular spectrum of the device at 1621 nm is shown in Figure 6-3(a). The Rayleigh angle for this wavelength is 4.4°. At the Rayleigh angle, the first-order substrate wave (T_1) starts propagating. The maximum energy transfer occurs at $\theta=4.72^{\circ}$ in this example, explicitly shown in Figure 6-3(b). The structure operates in the zero-order regime with only R_0 and T_0 for incident angles less than θ_R. At operating wavelengths other than 1621 nm, partial energy transfer takes place. Angular spectra at two different operating wavelengths of 1615 nm and 1630 nm are demonstrated in Figure 6-4(a) and (b), respectively. Sharp transitions in R_0 occur, but the sidebands are higher than for the 1621 nm wavelength. Hence we see that the desired filter response with 100% energy transfer is limited to a specific operating wavelength for a particular device design parameters. By tuning the values of Λ, F, d_g, d_h, n or n_s, the filter response can be designed for a required operating wavelength. For example, if the operating wavelength λ = 1550 nm is considered, then the Rayleigh reflector with parameters as Λ = 957 nm, F = 0.45, d_g = 310 nm and d_h = 55 nm, gives the angular spectral response with maximum energy transfer, as shown in Figure 6-5. The Rayleigh angle in this case is 6.87°.

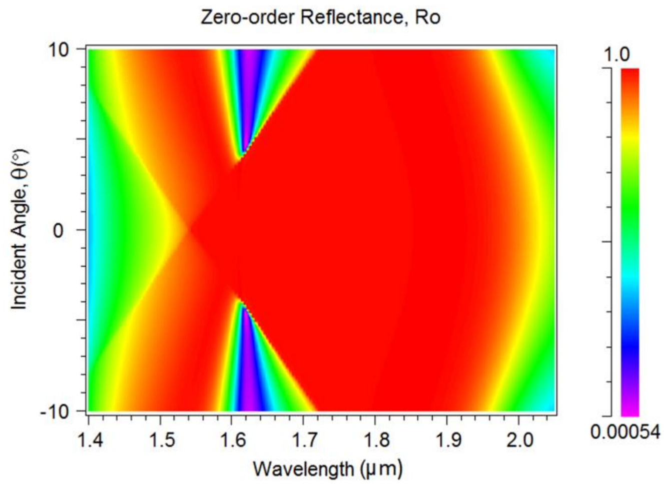

Figure 6-2 Zero-order reflectance map versus wavelength and incident angle for TE polarized light. Parameters are Λ = 1028 nm, F = 0.43, d_g = 319 nm, d_h = 60 nm, n_c = 1, n = 3.56 and n_s = 1.5.

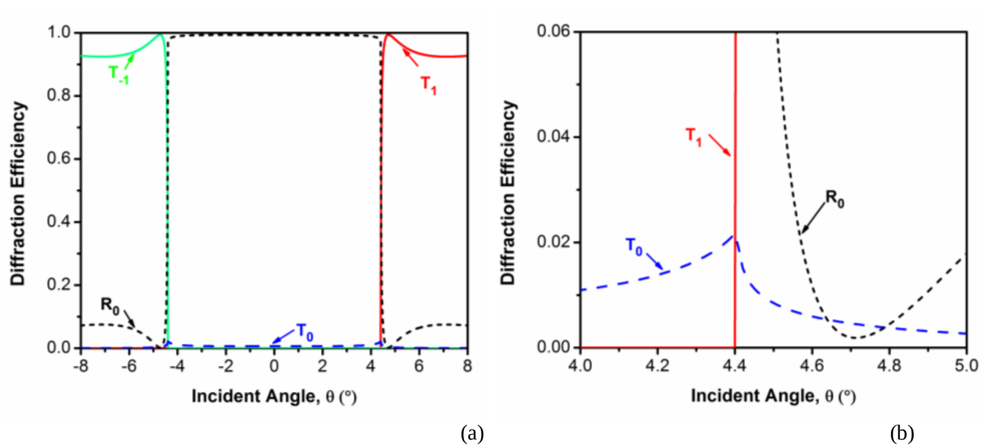

Figure 6-3 (a) Simulated angular spectrum for the Rayleigh reflector at λ= 1621 nm. Parameters are the same as in Figure 6-2, (b) magnified view at the onset of energy switch.

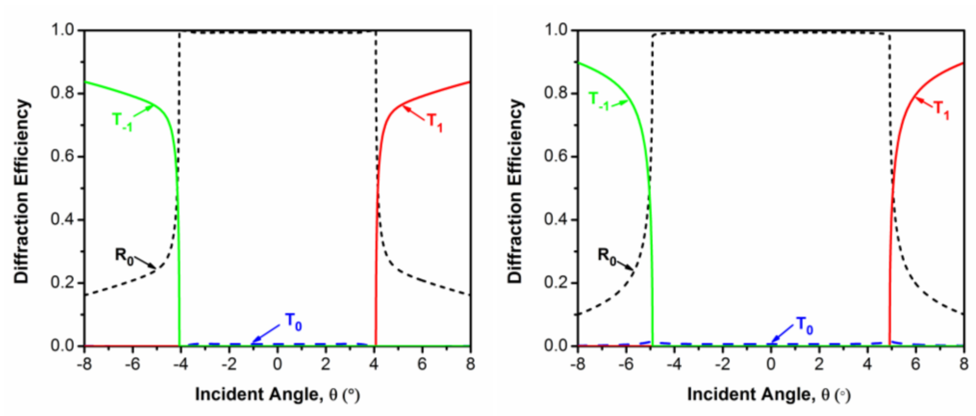

(a) (b)

Figure 6-4 Calculated angular spectrum for the Rayleigh reflector at (a) λ= 1615 nm, (b) λ= 1630 nm. Parameters are the same as in Figure 6-2.

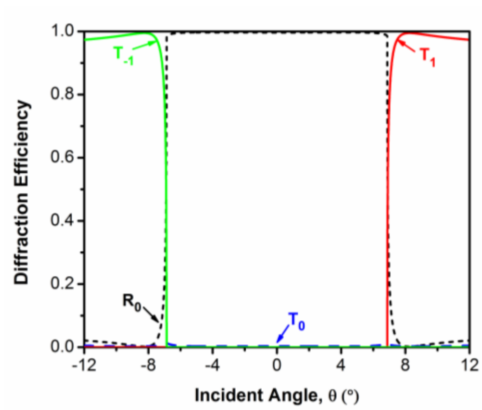

Figure 6-5 Simulated angular spectrum for Rayleigh reflector operating at λ = 1550 nm. Parameters are Λ = 957 nm, F = 0.45, d_g = 310 nm, d_h = 55 nm, n_c = 1, n = 3.56 and n_s = 1.5.

6.3 Theoretical Analysis

Fundamentally, the Rayleigh reflector works as a GMR broadband reflector in the spectral domain at normal incidence. The spectral response at $\theta = 0^{\circ}$ is shown in Figure 6-6(a) for the device parameters listed in Figure 6-2. The zero-order regime prevails beyond the Rayleigh wavelength, $\lambda_R = n_s\Lambda = 1548$ nm. For clarity, the T_0 spectrum is also drawn on a log scale to identify the transmission dip and the resonance wavelength. The GMR, occurring at 1902 nm wavelength, provides the high reflection bandwidth. In reference [10] it was shown that the Rayleigh reflector characteristics depend on direct and efficient transfer of power from R_0 to T_1 but not to T_0. In order to understand this property, we investigate the resonance dynamics of the present device under off-normal incidence. The key aspect of the Rayleigh reflector structure that leads to these sharply delimited angular spectra is that the structure supports a high-Q resonance near the RA at off-normal incidence. This is supported by the spectral response at $\theta = 2^{\circ}$ is given in Figure 6-6(b). An additional resonance occurs at 1611 nm wavelength whereas the RA occurs at 1577 nm at $\theta = 2^{\circ}$. The field amplitudes inside the structure at the 1902-nm resonance in Figure 6-6(a) and at the resonance at 1611 nm in Figure 6-6(b) are given in Figure 6-7(a) and (b), respectively. In the figure, S_0, S_1 and S_2 correspond to the electric-field amplitudes of the zeroth, first and second order diffracted waves, respectively. In Figure 6-7(b), the field strength increases by ~x15 relative to the incident light amplitude at the high-Q GMR occurring at off-normal incidence. With the increase in the incident angle, the RA and the high-Q GMR both exhibit red-shift in wavelength. However, the rate of shift of the RA (~20 nm/degree of θ) is comparatively higher than the rate of GMR shift. Accordingly, when the incident angle is increased, the RA interferes with the GMR in a particular angular range. When the RA reaches the GMR, the resonance dip in T_0 triggers energy switch from R_0 to the allowed propagating order T_1 associated with the RA. Eventually this results in a reflectance drop from unity to almost zero and a corresponding rise in the transmittance of the T_1–wave at a particular operating wavelength as shown in Figure 6-3.

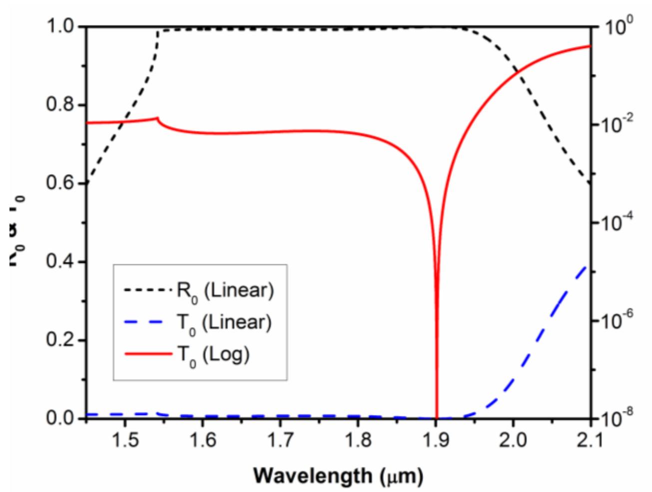

(a)

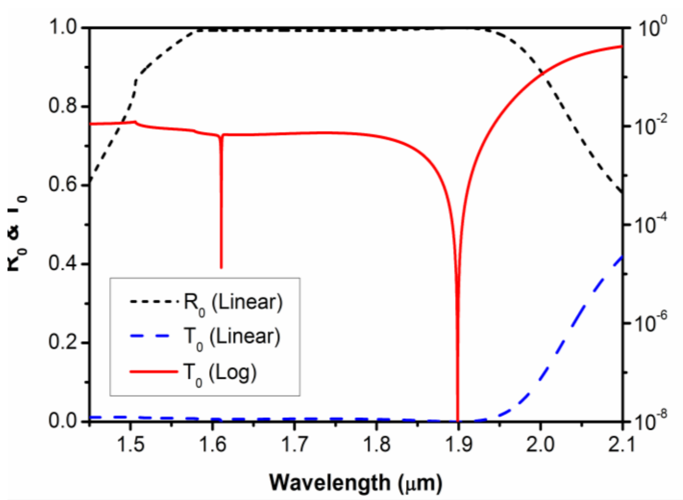

(b)

Figure 6-6 Computed spectral response of Rayleigh reflector at (a) $\theta = 0^{\circ}$ (b) $\theta = 2^{\circ}$. Parameters are Λ = 1028 nm, F = 0.43, d_g = 319 nm, d_h = 60 nm, n_c = 1, n = 3.56 and n_s = 1.5.

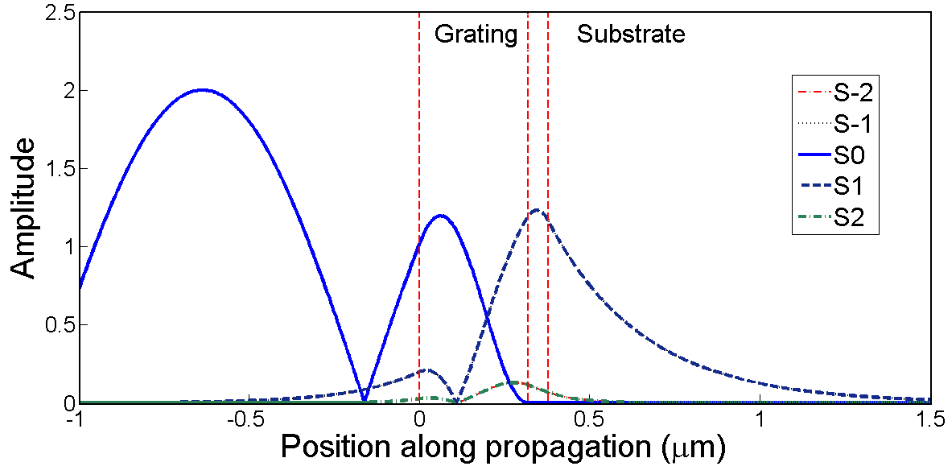

(a)

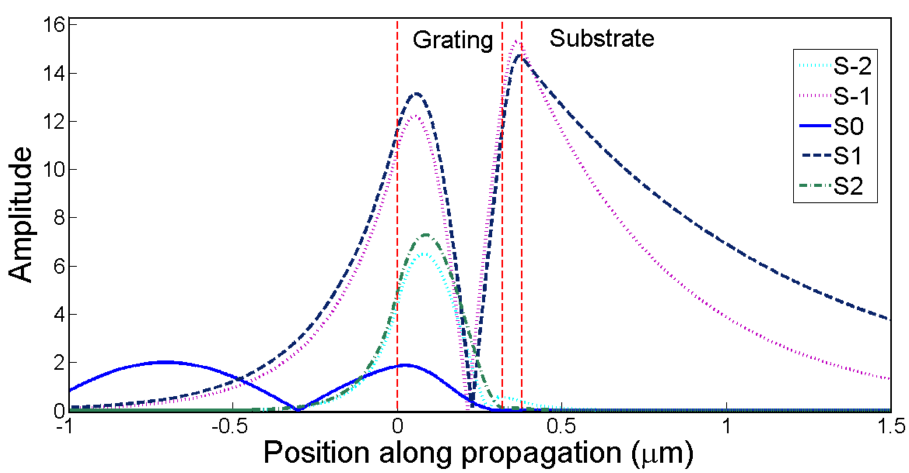

(b)

Figure 6-7 The field amplitudes inside the structure for (a) λ = 1902 nm at $\theta = 0^{\circ}$ and (b) λ = 1611 nm at $\theta = 2^{\circ}$.

6.4 Experiments

The fabrication of the Rayleigh reflector, schematically illustrated in Figure 6-8, commences with sputtering a-Si over a clean glass substrate. The refractive index and thickness of the film are verified with an ellipsometer. Approximately 400-nm-thick photoresist (PR) is spin coated over the silicon film. A one-dimensional grating pattern is transferred to the PR film using laser interferometric lithography. The a-Si layer is partially etched down to 319 nm with the PR as a mask using triflurомethane (CHF_3) and sulfur hexafluoride (SF_6) gas mixture. The final device is obtained after removing the remaining PR by oxygen plasma. The fabricated device is inspected with an atomic force microscope (AFM) and a scanning electron microscope (SEM). The AFM and SEM images are shown in Figure 6-9 and Figure 6-10, respectively. From the figures, the experimental parameters are Λ = 1028 nm, d_g = 319 nm, d_h = 60 nm and F = 0.43.

The reflected light from the device at different incident beam angles is measured with a spectrum analyzer. A polarizer is used to choose TE polarization of the input light. After measuring the reflected light from the Rayleigh reflector, it is normalized with respect to the reflected light from a reference gold mirror. Figures 6-11 (a-c) show the theoretical and experimental R_0 spectra at 0°, 3° and 5° incidence angles, respectively. Experimentally, a wideband reflector with spectral efficiency greater than 95% across a ~220nm wavelength range at normal incidence is obtained. The incident angle is varied from -8° to $+8^\circ$. The angular spectrum of the fabricated device is provided in Figure 6-12. A decrease in the R_0 efficiency is observed at $\theta = 4^\circ$ and maximum energy transfer is experimentally observed at $\theta = 5^\circ$. The wavelength at which this change is obtained is 1645 nm. The deviation in operating wavelength relative to the theoretical calculation can be attributed to differences in the experimental and model device parameters. Spectral measurements at angular intervals of 0.1 of a degree are necessary to observe a sharp response change as in simulation. Despite the deviations from the computed results, the Rayleigh-reflector concept with sharply varying angular spectra is verified.

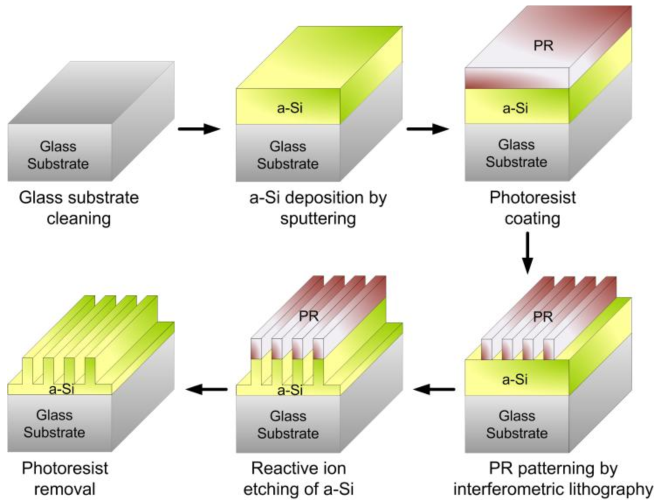

Figure 6-8 Schematic diagram of Rayleigh reflector fabrication.

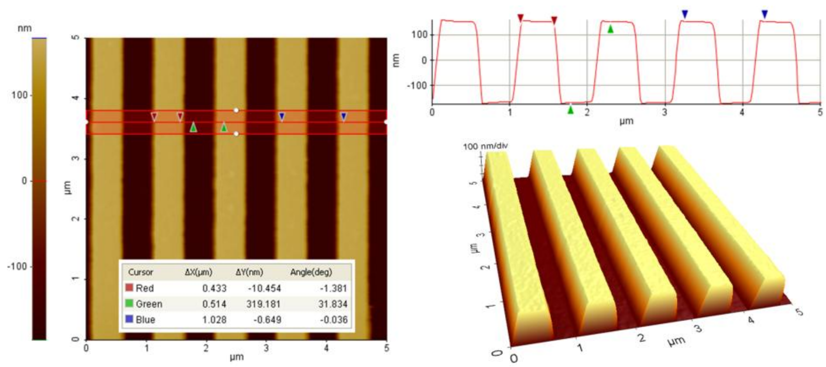

Figure 6-9 AFM image of fabricated Rayleigh reflector. Parameters are Λ = 1028 nm, F = 0.43, and d_g=319 nm.

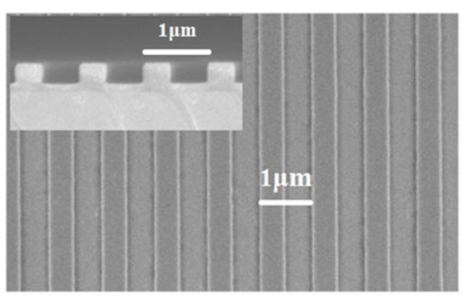

Figure 6-10 SEM top and cross-section images of fabricated Rayleigh reflector.

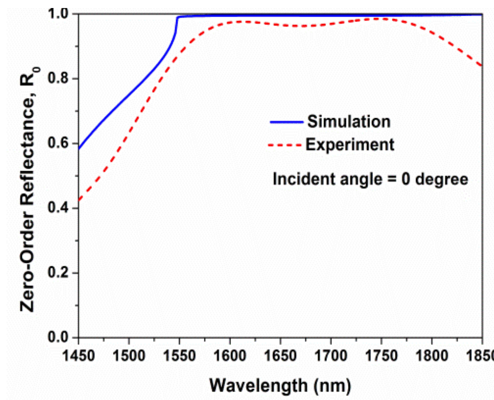

(a)

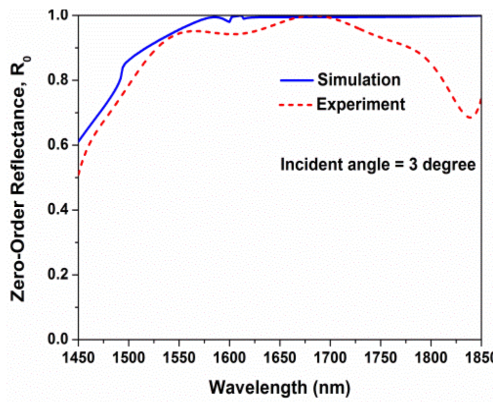

(b)

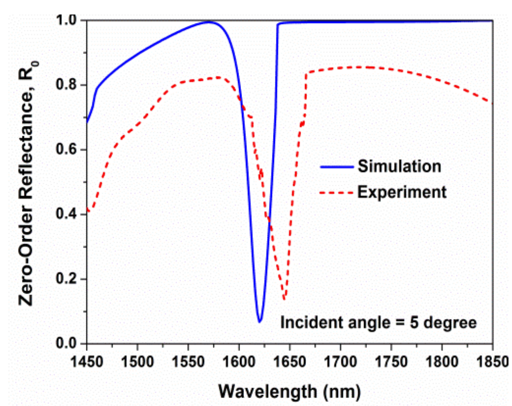

(c)

Figure 6-11 Calculated and experimental spectral response of the Rayleigh reflector for TE-polarized light at (a) $\theta = 0^{\circ}$, (b) $\theta = 3^{\circ}$ and (c) $\theta = 5^{\circ}$. Parameters: $d_g = 319$ nm, $d_h = 60$ nm, $n = 3.56$, $n_c = 1$, $n_s = 1.5$, $\Lambda = 1028$ nm, and $F = 0.43$.

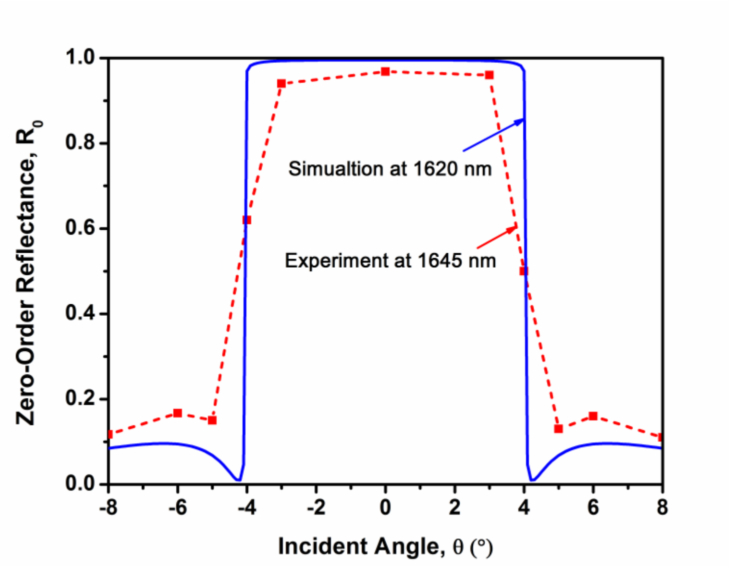

Figure 6-12 Calculated and experimental angular spectra of a Rayleigh reflector.

6.5 Conclusions

The combined effect of RA and GMR possess capability of creating extraordinary photonic phenomena. The working principle of a novel optical filter named Rayleigh reflector has been analyzed and experimentally verified. A subwavelength, periodic one-dimensional silicon grating pattern and a nanometric sublayer over glass substrate exhibit flat-top reflector profile with sharply limited angular spectra. The onset of extreme energy transfer from the zero-order reflected wave to the first-order substrate propagating wave occurs at the Rayleigh angle enabled by the RA-GMR interaction. The designed structure is fabricated and an agreement with theoretical prediction is achieved. The theoretical analysis and experimental proof leads to the realization of a new type of resonant reflector in diversified photonic applications.

Chapter 7

Future Research Directions

The research works presented in this study can be carried on in extended platforms. Some of the possibilities are summarized below:

- Optimized resonant solar cells design and fabrication:

  The nano-structured thin-film solar cells require optimization of the device parameters to achieve maximum solar absorption. The structural shape and parameters should be optimized in such a way that it gives maximized carrier collection as well. Combination of enhanced absorbance and efficient photo-generated carrier collection is required for increased electrical efficiency. Cost-effective thin-film solar cells with increased efficiency are the ultimate target.

- Fabrication of thin-film solar cells on imprinted plexiglas:

  The enhanced absorption in one and two dimensional thermally nano-imprinted structures is reported here. The deposition of complete p-i-n a-Si:H solar cells on these imprinted substrates can be carried out to make a real device application.

- Application in thin-film organic solar cells:

  The nano-structures presented here are also hold potential to enhance solar uptake in thin-film organic solar cells. The consecutive spin coating of organic materials over the nano-patterned substrates will similarly facilitate the resonances in the active region of organic photovoltaics.

- Research on Rayleigh reflector:

  A whole new research field has been initiated for the design and applications of the Rayleigh reflectors. The two dimensional and/or multilayer structures may add interesting spectral responses in Rayleigh reflectors. The application of the Rayleigh reflector concept can lead to a new way of designing couplers, filters and reflectors in silicon photonics.

Appendix A

List of Publications

Journals

[1] **T. Khaleque** and R. Magnusson, “Light management through guided-mode resonances in thin-film silicon solar cells”, J. of Nanophotonics, vol. 8, 083995 (1-8) 2014.

[2] **T. Khaleque**, H. G. Svavarsson and R. Magnusson, “Fabrication of resonant patterns using thermal nano-imprint lithography for thin-film photovoltaic applications,” Optics Express-Energy, vol. 21, no. S4, pp. A631-A641, July 2013.

[3] **T. Khaleque**, M. J. Uddin and R. Magnusson, “Design and fabrication of wideband guided-mode resonant reflectors in TE polarization,” Optics Express, 2014 (Accepted).

[4] **T. Khaleque**, M. J. Uddin and R. Magnusson, “Theory and experiment of flat-top optical filter enabled by Rayleigh anomaly,” Optics Express, 2014 (To be submitted).

[5] M. J. Uddin, **T. Khaleque** and R. Magnusson, "Guided-mode resonant polarization controlled tunable color filters," Optics Express, 2014 (under review).

Conference Proceedings

[1] R. Magnusson, J. W. Yoon, M. S. Amin, **T. Khaleque** and M. J. Uddin, "Extraordinary capabilities of optical devices incorporating guided-mode resonance gratings: application summary and recent examples,” in the Proc. of *SPIE Photonics West,* vol. 8988, pp. 89880I (1-10), San Francisco, California, February 1–6, 2014.

[2] **T. Khaleque**, H. G. Svavarsson and R. Magnusson, “Fabrication of nano-imprinted resonant structures for thin-film solar cell applications,” in the Proc. of *IEEE Photonics Conference*, paper WH4.5, Bellevue, Washington, September 8-12, 2013.

[3] R. Magnusson, **T. Khaleque** and M. J. Uddin, "Optical filters enabled by Rayleigh anomaly: theory and experiment," in the Proc. of *IEEE Photonics Conference*, paper TuH3.3, Bellevue, Washington, September 8-12, 2013.

[4] **T. Khaleque** and R. Magnusson, “Experiments with resonant thin-film hydrogenated amorphous silicon solar cells,” in the Proc. of *Solar Energy & Technology, SPIE Optics+Photonics*, vol. 8470, pp. 847008 (1-8), San Diego, California, August 12–16, 2012.

[5] **T. Khaleque**, J. Yoon, W. Wu, and R. Magnusson, “Absorption enhancement in guided-mode-resonant hydrogenated amorphous silicon thin-film solar cells,” in the Proc. of *Optics and Photonics Congress: Renewable Energy and the Environment*, paper PWD3, Austin, Texas, November 2-4, 2011.

[6] **T. Khaleque**, J. Yoon, W. Wu, M. Shokooh-Saremi, and R. Magnusson, “Guided-mode-resonance enabled absorption in amorphous silicon for thin-film solar cell applications”, in the Proc. of Integrated *Photonics Research*, paper ITuD3, Toronto, Canada, June 12-16, 2011.

Poster

[1] **T. Khaleque** and R. Magnusson, “Photocurrent enhancement in resonant thin-film hydrogenated amorphous silicon solar cells”, *Power and Energy Systems, IEEE MetroCon*, Arlington, Texas, October 11, 2012 (Awarded “Best Graduate Student Poster Presentation”).

References

Chapter 1

[1] P. Vincent and M. Neviere, “Corrugated dielectric waveguides: A numerical study of the second-order stopbands,” Appl. Phys. **20**, 345-351 (1979).

[2] L. Mashev and E. Popov, “Zero order anomaly of dielectric coated gratings,” Opt. Comm. **55**, 377-380 (1985).

[3] G. A. Golubenko, A. S. Svakhin, V. A. Sychugov and A. V. Tishchenko, “Total reflection of light from a corrugated surface of a dielectric waveguide,” Sov. J. Quantum Electron. **15**, 886-887 (1985).

[4] I. A. Avrutsky and V. A. Sychugov, “Reflection of a beam of finite size from a corrugated waveguide,” J. Mod. Opt. **36**, 1527-1539 (1989).

[5] S. S. Wang, R. Magnusson, J. S. Bagby and M. G. Moharam, “Guided-mode resonances in planar dielectric layer diffraction gratings,” J. Opt. Soc. Am. A **7**, 1470-1474 (1990).

[6] R. Magnusson and S. S. Wang, “New principle for optical filters,” Appl. Phys. Lett. **61**, 1022-1024 (1992).

[7] S. S. Wang and R. Magnusson, “Theory and applications of guided-mode resonance filters,” Appl. Opt. **32**, 2606-2613 (1993).

[8] S. S. Wang and R. Magnusson, “Multilayer waveguide-grating filters,” Appl. Opt. **34**, 2414-2420 (1995).

[9] M. T. Gale, K. Knop, and R. Morf, “Zero-order diffractive microstructures for security applications,” Proc. SPIE **1210**, 83-89 (1990).

[10] D. Rosenblatt, A. Sharon, and A. A. Friesem, “Resonant grating waveguide structures,” IEEE J. Quantum Electron. **33**, 2038-2059 (1997).

[11] D. L. Brundrett, E. N. Glytsis and T. K. Gaylord, “Normal-incidence guided-mode resonant grating filters: design and experimental demonstrations,” Opt. Lett. **23**, 700-702 (1998).

[12] P. S. Priambodo, T. A. Maldonado and R. Magnusson, “Fabrication and characterization of high-quality waveguide-mode resonant optical filters,” Appl. Phys. Lett. **83**, 3248-3250 (2003).

[13] Y. Ding and R. Magnusson, “Resonant leaky-mode spectral-band engineering and device applications,” Opt. Express **12**, 5661-5674 (2004).

[14] C. F. R. Mateus, M. C. Y. Huang, Y. Deng, A. R. Neureuther, and C. J. Chang-Hasnain, “Ultrabroadband mirror using low-index cladded subwavelength grating,” IEEE Photonics Technol. Lett. **16**, 518-520 (2004).

[15] C. F. R. Mateus, M. C. Y. Huang, L. Chen, C. J. Chang-Hasnain and Y. Suzuki, “Broad-band mirror (1.12–1.62μm) using a subwavelength grating,” IEEE Photon. Technol. Lett. **16**, 1676-1678 (2004).

[16] C. -L. Hsu, Y. -C. Liu, C.-M. Wang, M. -L. Wu, Y. -L. Tsai, Y. -H., Chou, C. -C. Lee and J. -Y. Chang, “Bulkmicromachined optical filter based on guided-mode resonance in silicon-nitride membrane,” J. Lightwave Technol. **24**, 1922-1928 (2006).

[17] Y. Kanamori, T. Kitani and K. Hane, “Guided-mode resonant grating filter fabricated on silicon-on-insulator substrate,” Jpn. J. Appl. Phys. **45**, 1883-1885 (2006).

[18] A. Sentenac and A. L. Fehrembach, “Angular tolerant resonant grating filters under oblique incidence,” J. Opt. Soc. Am. A **22**, 475-480 (2005).

[19] A. -L. Fehrembach, A. Talneau, O. Boyko, F. Lemarchand and A. Sentenac, "Experimental demonstration of a narrowband, angular tolerant, polarization independent, doubly periodic resonant grating filter," Opt. Lett. **32**, 2269-2271 (2007).

[20] K. J. Lee, R. LaComb , B. Britton, M. Shokooh-Saremi, H. Silva, E. Donkor, Y. Ding and R. Magnusson, "Silicon-layer guided-mode resonance polarizer with 40 nm bandwidth," IEEE Photon. Technol. Lett. **20**, 1857-1859 (2008).

[21] K. J. Lee, J. H. Jin, B.-S. Bae and R. Magnusson, "Optical filters fabricated in hybrimer media with soft lithography," Opt. Lett. **34**, 2510-2512 (2009).

[22] R. Magnusson and Y. Ding, "MEMS tunable resonant leaky mode filters," IEEE Photon. Technol. Lett. **18**, 1479-1481 (2006).

[23] R. Magnusson and M. Shokooh-Saremi, "Widely tunable guided-mode resonance nanoelectromechanical RGB pixels," Opt. Express **15**, 10903-10910 (2007).

[24] Y. Ding and R. Magnusson "Band gaps and leaky-wave effects in resonant photonic-crystal waveguides," Opt. Express **15**, 680-694 (2007).

[25] R. Magnusson, Y. Ding, K. J. Lee, D. Shin, P. S. Priambodo, P. P. Young and T. A. Maldonado, "Photonic devices enabled by waveguide-mode resonance effects in periodically modulated films," Proc. SPIE **5225**, 20-34 (2003).

[26] S. S. Wang and R. Magnusson, "Design of waveguide-grating filters with symmetric line shapes and low side-bands," Opt. Lett. **19**, 919-921 (1994).

[27] R. Magnusson and S. S. Wang, "Transmission bandpass guided-mode resonance filters," Appl. Opt. **34**, 8106-8109 (1995).

[28] S. Tibuleac, and R. Magnusson, "Diffractive narrow-band transmission filters based on guided-mode resonance effect in thin-film multilayers," IEEE Photon. Technol. Lett. **9**, 464-467(1997).

[28] Z. S. Liu, S. Tibuleac, D. Shin, P. P. Young, and R. Magnusson, “High-efficiency guided-mode resonance filter,” Opt. Lett. **23**, 1556-1558 (1998).

[29] D. Shin, S. Tibuleac, T. A. Maldonado, and R. Magnusson, “Thin-film optical filters with diffractive elements and waveguides,” Opt. Engg. **37**, 2634-2646 (1998).

[30] S. Tibuleac, R. Magnusson, P. P. Young and T. R. Holzheimer, “Experimental verification of waveguide-mode resonant transmission filters,” IEEE Microwave and Guided Wave Lett. **9**, 19-21(1999).

[31] S. Tibuleac and R. Magnusson, “Narrow-linewidth bandpass filters with diffractive thin-film layers,” Opt. Lett. **26**, 584-586 (2001).

[32] Y. ding and R. Magnusson, "Use of nondegenerate resonant leaky modes to fashion diverse optical spectra," Opt. Express **12**, 1885-1891 (2004).

[33] M. S. Amin, J. W. Yoon and R. Magnusson, “Optical transmission filters with co-existent guided-mode resonance and Rayleigh anomaly,” Appl. Phys. Lett. **103**, 131106 (2013).

[34] R. Magnusson, P. P. Young and D. Shin, “Vertical-cavity laser and laser array incorporating guided-mode resonance effects and methods for making the same,” US Patent No. 6154480 (2000).

[35] K. J. Lee, J. Curzan, M. Shokooh-Saremi, and R. Magnusson, “Resonant wide-band polarizer with single silicon layer,” Appl. Phys. Lett. **98**, 211112 (2011).

[36] R. Magnusson and M. Shokooh-Saremi, “Physical basis for wideband resonant reflector,” Opt. Express **16**, 3456-3462 (2008).

[37] M. Shokooh-Saremi and R. Magnusson, "Wideband leaky-mode resonance reflectors: influence of grating profile and sublayers," Opt. Express **16**, 18249-18263 (2008).

[38] K. J. Lee and R. Magnusson, “Single-layer resonant high reflector in TE polarization: Theory and Experiment,” IEEE Photon. J. **3**, 123-129 (2011).

[39] M. J. Uddin and R. Magnusson, “Efficient guided-mode resonant tunable color filters,” IEEE Photon. Technol. Lett. **24**, 1552-1554 (2012).

[40] M. J. Uddin and R. Magnusson, “Highly efficient color filter array using resonant Si_3N_4 gratings,” Opt. Express **21**, 12495 -12506 (2013).

[41] M. J. Uddin and R. Magnusson, “Guided-mode resonant thermo-optic tunable filters, IEEE Photon. Technol. Lett. **25**, 1412-1415 (2013).

[42] S. Kaja, J. D. Hilgenberg, J. L. Collins, A. A. Shah, D. Wawro, S. Zimmerman, R. Magnusson and P. Koulen, "Detection of novel biomarkers for ovarian cancer with an optical nanotechnology detection system enabling label-free diagnostics," J. Biomed. Optics **17**, 081412 (1-8) (2012).

[43] R. Magnusson, “The complete biosensor,” J. Biosensors and Bioelectronics **4**, 1-2(2013).

[44] T. Khaleque and R. Magnusson, “Light management through guided-mode resonances in thin-film silicon solar cells”, J. of Nanophotonics 8, 083995 (1-13) (2014).

[45] T. Khaleque, H. G. Svavarsson and R. Magnusson, “Fabrication of resonant patterns using thermal nano-imprint lithography for thin-film photovoltaic applications,” Optics Express-Energy **21**, A631-A641 (2013).

[46] R. Magnusson, “Flat-top resonant reflectors with sharply delimited angular spectra: an application of the Rayleigh anomaly” Opt. Lett. **38**, 989-991(2013).

[47] R. Magnusson, T. Khaleque and M. J. Uddin, "Optical filters enabled by Rayleigh anomaly: theory and experiment," in the Proc. of IEEE Photon. Conf. TuH3.3, 335-336 (2013).

[48] R. Magnusson, J. W. Yoon, M. S. Amin, T. Khaleque and M. J. Uddin, "Extraordinary capabilities of optical devices incorporating guided-mode resonance gratings: application summary and recent examples," in the Proc. of SPIE **8988**, 89880I (1-10) (2014).

[49] T. K. Gaylord and M. G. Moharam, "Analysis and application of optical diffraction by gratings," Proc. of the IEEE **73**, 894-936 (1985).

Chapter 2

[1] C. Heine and R. H. Morf, "Submicrometer gratings for solar energy applications," Appl. Opt. 34, 2476-2482 (1995).

[2] M. Kroll, S. Fahr, C. Helgert, C. Rockstuhl, F. Lederer, and T. Pertsch, "Employing dielectric diffractive structures in solar cells-a numerical study," Phys. Stat. Sol. (a) 205, 2777-2795 (2008).

[3] J. G. Mutitu, S. Shi, C. Chen, T. Creazzo, A. Barnett, C. Honsberg, and D. W. Prather, "Thin film silicon solar cell design based on photonic crystal and diffractive grating structures," Opt. Express 16, 15238-15248 (2008).

[4] Y. -C. Lee, C. -F. Huang, J. -Y. Chang, and M. -L. Wu, "Enhanced light trapping based on guided mode resonance effect for thin film solar cells with two filling-factor gratings," Opt. Express 16, 7969-7975 (2008).

[5] K. Yamamoto, A. Nakajima, M. Yoshimi, T. Sawada, S. Fukuda, T. Suezaki, M. Ichikawa, Y. Koi, M. Goto, T. Meguro, T. Matsuda, M. Kondo, T. Sasaki, and Y. Tawada, "A high efficiency thin film silicon solar cell and module," Solar Energy 77, 939-949 (2004).

[6] L. Zeng, P. Bermel, Y. Yi, B. A. Alamariu, K. A. Broderick, J. Liu, C. Hong, X. Duan, J. Joannopoulos, and L. C. Kimerling, "Demonstration of enhanced absorption in

thin film Si solar cells with textured photonic crystal back reflector," Appl. Phys. Lett. 93, 221105-1–221105-3 (2008).

[7] L. Zhao, Y. H. Zuo, C. L. Zhou, H. L. Li, H. W. Diao, and W. J. Wang, "A highly efficient light-trapping structure for thin-film silicon solar cells," Solar Energy 84, 110-115 (2010).

[8] Y. Park, E. Drouard, O. E. Daif, X. Letartre, P. Viktorovitch, A. Fave, A. Kaminski, M. Lemiti, and C. Seassal, "Absorption enhancement using photonic crystals for silicon thin film solar cells," Opt. Express 17, 14312-14321 (2009).

[9] J. Gjessing, E. S. Marstein, and A. Sudbø, "2D back-side diffraction grating for improved light trapping in thin silicon solar cells," Opt. Express 18, 5481-5495 (2010).

[10] Y. M. Song, J. S. Yu, and Y. T. Lee, "Antireflective submicrometer gratings on thin-film silicon solar cells for light-absorption enhancement," Opt. Lett. 35, 276-278 (2010).

[11] R. Magnusson and S. S. Wang, "New Principle for optical filters," Appl. Phys. Lett. **61**, 1275-1297 (1992).

[12] S. S. Wang and R. Magnusson, "Theory and applications of guided-mode resonance filters," Appl. Opt. **32**, 2606-2613(1993).

[13] D. Shin, S. Tibuleac, T. A. Maldonado, and R. Magnusson, "Thin-film optical filters with diffractive elements and waveguides," Opt. Engg. **37**, 2634-2646 (1998).

[14] D. Rossenblatt, A. Sharon, and A. A. Friesem, "Resonant grating waveguide structure," IEEE J. Quant. Electron. **33**, 2038-2058 (1997).

[15] Y. ding and R. Magnusson, "Resonant leaky-mode spectral band engineering and device applications," Opt. Express. **12**, 5661-5674 (2004).

[16] T. K. Gaylord and M. G. Moharam, "Analysis and application of optical diffraction by gratings," Proc. of the IEEE **73**, 894-936 (1985).

[17] M. J. Uddin and R. Magnusson, "Highly efficient color filter array using resonant Si_3N_4 gratings," Opt. Express **21**, 12495 -12506 (2013).

Chapter 3

[1] M. A. Green, "Thin-film solar cells: review of materials, technologies and commercial status," J. Mater. Sci: Mater. Electron. **18**, S15-S19 (2007).

[2] A. V. Shah, H. Schade, M. Vanecek, J. Meier, E. V. Sauvain, N. Wyrsch, U. Kroll, C. Droz, and J. Bailat, "Thin-film silicon solar cell technology," Prog. Photovolt: Res. Appl. **12**, 113-142 (2004).

[3] S. B. Mallick, N. P. Sergeant, M. Agrawal, J.-Y. Lee, and P. Peumans, "Coherent light trapping in thin-film photovoltaics," MRS Bulletin **36**, 453-460 (2011).

[4] C. Heine and R. H. Morf, "Submicrometer gratings for solar energy applications," Appl. Opt. **34**, 2476-2482 (1995).

[5] N.-N. Feng, J. Michel, L. Zeng, J. Liu, C.-Y. Hong, L. C. Kimerling, and X. Duan, "Design of highly efficient light-trapping structures for thin-film crystalline silicon solar cells," IEEE Trans. Electron. Devices **54**, 1926-1933 (2007).

[6] M. Kroll, S. Fahr, C. Helgert, C. Rockstuhl, F. Lederer, and T. Pertsch, "Employing dielectric diffractive structures in solar cells-a numerical study," Phys. Stat. Sol. (a) **205**, 2777-2795 (2008).

[7] J. Muller, B. Rech, J. Springer, and M. Vanecek, "TCO and light trapping in silicon thin-film solar cells," Solar Energy **77**, 917-930 (2004).

[8] K.-C. Lai, F.-J. Tsai, J.-H. Wang, C.-H. Yeh, and M.-P. Houng, “Texturing of the back reflector for light trapping enhancement in micromorph thin film solar cells,” Thin Solid Films **519**, 3946-3949 (2011).

[9] S.-S. Lo, C.-C. Chen, F. Garwe, and T. Pertch, “Broad-band anti-reflection coupler for a:Si thin-film solar cell,” J. of Phys. D: Appl. Phys. **40**, 754-758 (2007).

[10] Y. M. Song, J. S. Yu, and Y. T. Lee, “Antireflective submicrometer gratings on thin-film silicon solar cells for light-absorption enhancement,” Opt. Lett. **35**, 276-278 (2010).

[11] H. A. Atwater and A. Polman, “Plasmonics for improved photovoltaic devices,” Nature Materials **9**, 205-213 (2010).

[12] H.-Y. Lin, Y. Kuo, C.-Y. Liao, C. C. Yang, and Y.-W. Kiang, “Surface plasmon effects in the absorption enhancements of amorphous silicon solar cells with periodical metal nanowall and nanopillar structures,” Opt. Express **20**, 104-118 (2011).

[13] S. Y. Chou and W. Ding, “Ultrathin, high-efficiency, broad-band, omni-acceptance, organic solar cells enhanced by plasmonic cavity with subwavelength hole array,” Opt. Express **21**, A60-A76 (2013).

[14] J. G. Mutitu, S. Shi, C. Chen, T. Creazzo, A. Barnett, C. Honsberg, and D. W. Prather, “Thin film silicon solar cell design based on photonic crystal and diffractive grating structures,” Opt. Express **16**, 15238-15248 (2008).

[15] L. Zeng, P. Bermel, Y. Yi, B. A. Alamariu, K. A. Broderick, J. Liu, C. Hong, X. Duan, J. Joannopoulos, and L. C. Kimerling, “Demonstration of enhanced absorption in thin-film Si solar cells with textured photonic crystal back reflector,” Appl. Phys. Lett. **93**, 221105 (2008).

[16] B. Curtin, R.Biswas and V. Dalal, “Photonic crystal based back reflectors for light management and enhanced absorption in amorphous silicon solar cells,” Appl. Phys. Lett. **95**, 231102 (2009).

[17] Y.-C. Lee, C.-F. Huang, J.-Y. Chang, and M.-L. Wu, “Enhanced light trapping based on guided mode resonance effect for thin-film solar cells with two filling-factor gratings,” Opt. Express **16**, 7969-7975 (2008).

[18] K. Söderström, F.-J. Haug, J. Escarré, O. Cubero, and C. Ballif, “Photocurrent increase in n-i-p thin-film silicon solar cells by guided mode excitation via grating coupler,” Appl. Phys. Lett. **96**, 213508 (2010).

[19] E. Garnett and P. Yang, “Light trapping in silicon nanowire solar cells,” Nano Lett. **10**, 1082-1087 (2010).

[20] J. Zhu, C. M. Hsu, Z. Yu, S. Fan, and Y. Cui, “Nanodome solar cells with efficient light management and self-cleaning,” Nano Lett. **10**, 1979-1984 (2010).

[21] J. Kim, A. J. Hong, J.-W. Nah, B. Shin, F. M. Ross, and D. K. Sadana, “Three-dimensional a-Si:H solar cells on glass nanocone arrays patterned by self-assembled Sn nanospheres,” ACS Nano **6**, 265-271 (2012).

[22] A. Fontcuberta i Morral and P. Roca i Cabarrocas, “Structure and hydrogen content of polymorphous silicon thin films studied by spectroscopic ellipsometry and nuclear measurements,” Phys. Rev. B **69**, 125307 (2004).

Chapter 4

[1] Y. M. Song, J. S. Yu, and Y. T. Lee, “Antireflective submicrometer gratings on thin-film silicon solar cells for light-absorption enhancement,” Opt. Lett. **35**, 276-278 (2010).

[2] H. A. Atwater and A. Polman, “Plasmonics for improved photovoltaic devices,” Nature Materials **9**, 205-213 (2010).

[3] Y.-C. Lee, C.-F. Huang, J.-Y. Chang, and M.-L. Wu, “Enhanced light trapping based on guided mode resonance effect for thin-film solar cells with two filling-factor gratings,” Opt. Express **16**, 7969-7975 (2008).

[4] J. Zhu, C. M. Hsu, Z. Yu, S. Fan, and Y. Cui, “Nanodome solar cells with efficient light management and self-cleaning,” Nano Lett. **10**, 1979-1984 (2010).

[5] E. Garnett and P. Yang, “Light trapping in silicon nanowire solar cells,” Nano Lett. **10**, 1082-1087 (2010).

[6] J. Kim, A. J. Hong, J.-W. Nah, B. Shin, F. M. Ross, and D. K. Sadana, “Three-dimensional a-Si:H solar cells on glass nanocone arrays patterned by self-assembled Sn nanospheres,” ACS Nano **6**, 265-271 (2012).

[7] K.-J. Byeon and H. Lee, “Recent progress in direct patterning technologies based on nano-imprint lithography,” Eur. Phys. J. Appl. Phys. **59**, 10001 (2012).

[8] S. Y. Chou. P. R. Krauss, and P. J. Renstrom, “Imprint of sub-25nm vias and trenches in polymers,” Appl. Phys. Lett. **67**, 3114-3116 (1995).

[9] K.-S. Han, S.-H. Hong, and H. Lee, “Fabrication of complex nanoscale structures on various substrates,” Appl. Phys. Lett. **91**, 123118 (2007).

[10] S. Y. Chou, C. Keimel, and J. Gu, “Ultrafast and direct imprint of nanostructures in silicon,” Nature **417**, 835-837 (2002).

[11] C.-J. Ting, M.-C. Huang, H.-Y. Tsai, C.-P. Chou, and C.-C. Fu, “Low cost fabrication of the large-area anti-reflection films from polymer by nanoimprint/hot-embossing technology,” Nanotechnology **19**, 205301 (2008).

[12] J. Y. Chen and K. W. Sun, "Enhancement of the light conversion efficiency of silicon solar cells by using nanoimprint anti-reflection layer," Sol. Ener. Mat. and Sol. Cells **94**, 629-633 (2010).

[13] K.-S. Han, J.-H. Shin, W.-Y. Yoon, and H. Lee, "Enhanced performance of solar cells with anti-reflection layer fabricated by nano-imprint lithography," Sol. Ener. Mat. and Sol. Cells **95**, 288-291 (2011).

[14] S.-J. Liu and C.-T. Liao, "Fast fabrication of nano-structured anti-reflection layers for enhancement of solar cells performance using plasma sputtering and infrared assisted roller embossing techniques," Optics Express **20**, 5143-5150 (2012).

[15] M. Fonrodona. J. Escarré, F. Villar, D. Soler, J. M. Asensi, J. Bertomeu, and J. Andreu, "PEN as substrate for new solar cell technology," Sol. Ener. Mat. and Sol. Cells **89**, 37-47 (2005).

[16] A. Bessonov, Y. Cho, S. –J. Jung, E. –A. Park, E. –S. Hwang, J. –W. Lee, M. Shin, and S. Lee, "Nanoimprint patterning for tunable light trapping in large-area silicon solar cells," Sol. Ener. Mat. and Sol. Cells **95**, 2886-2892 (2011).

[17] K. Söderström, J. Escarré, O. Cubero, F. –J. Haug, S. Perregaux, and C. Ballif, "UV-nano-imprint lithography technique for the replication of back reflectors for n-i-p thin film silicon solar cells," Prog. Photvolt: Res. Appl. **19**, 202-210 (2011).

[18] V. E. Ferry, M. A. Verschuuren, M. C. van Lare, R. E. I. Schropp, H. A. Atwater, and A. Polman, "Optimized spatial correlations for broadband light trapping nanopatterns in high efficiency ultrathin film a-Si:H solar cells," Nano Lett. **11**, 4239-4245 (2011).

[19] C. Battaglia, J. Escarré, K. Söderström, M. Charrière, M. Despeisse, F. –J. Haug, and C. Ballif, "Nanomoulding of transparent zinc oxide electrodes for efficient light trapping in solar cells," Nature Photonics Lett. **5**, 535-538 (2011).

[20] T. Khaleque and R. Magnusson, "Experiments with resonant thin-film hydrogenated amorphous silicon solar cells," Proc. SPIE **8470**, 847008 (2012).

[21] R. M. Waxler, D. Horowitz, and A. Feldman, "Optical and physical parameters of plexiglas 55 and lexan," Appl. Opt. **18**, 101-104 (1979).

[22] W. Wu and R. Magnusson, "Total absorption of TM polarized light in a 100nm spectral band in a nanopatterned thin a-Si film," Opt. Lett. **37**, 2103-2105 (2012).

[23] T. K. Gaylord and M. G. Moharam, "Analysis and applications of optical diffraction by gratings," Proc. of the IEEE, **73**, 894-937 (1985).

Chapter 5

[1] P. Cheben, S. Janz, D. -X. Xu, B. Lamontagne, A. Delâge, and S. Tanev, "A broad-band waveguide grating coupler with a subwavelength grating mirror," IEEE Photon. Technol. Lett. 18, 13-15 (2006).

[2] C. C. Wang and S. D. Lin, "Resonant cavity-enhanced quantum-dot infrared photodetectors with sub-wavelength grating mirror," J. Appl. Phys. 113, 213108 (2013).

[3] M. C. Y. Huang, Y. Zhou, and C. J. Chang-Hasnain, "A surface-emitting laser incorporating a high-index contrast subwavelength grating," Nature Photon. 1, 119-122 (2007).

[4] M. A. Ahmed, M. Rumpel, A. Voss, and T. Graf, "Applications of sub-wavelength grating mirrors in high-power lasers," Adv. Opt. Techn. 1, 381-388 (2012).

[5] C. F. R. Mateus, M. C. Y. Huang, Y. Deng, A. R. Neureuther, and C. J. Chang-Hasnain, "Ultrabroadband mirror using low-index cladded subwavelength grating," IEEE Photon. Technol. Lett. 16, 518-520 (2004).

[6] Y. Ding and R. Magnusson, "Resonant leaky-mode spectral-band engineering and device applications," Opt. Express 12, 5661-5674 (2004).

[7] H. Wu, L. Huang, Y. Xiao, C. Zhang, S. Li, N. Luo, X. He, and Y. Gao, "A wideband reflector realized by a subwavelength multi-subpart profile grating structure," J. Opt. 15, 035703 (1-5) (2013).

[8] H. Wu, J. Hou, W. Mo, D. Gao, and Z. Zhou, "A multilayer-based high-performance multisubpart profile grating reflector," IEEE Photon. Technol. Lett. 22, 203-205 (2010).

[9] K. J. Lee and R. Magnusson, "Single-layer resonant high reflector in TE polarization: Theory and experiment," IEEE Photon. J. 3, 123-129 (2011).

[10] R. Magnusson and M. Shokooh-Saremi, "Physical basis for wideband resonant reflectors," Opt. Express 16, 3456-3462 (2008).

[11] M. Shokooh-Saremi and R. Magnusson, "Wideband leaky-mode resonance reflectors: Influence of grating profile and sublayers," Opt. Express 16, 18249-18263 (2008).

[12] R. Magnusson, "Flat-top resonant reflectors with sharply delimited angular spectra: an application of the Rayleigh anomaly," Opt. Lett. 38, 989-991 (2013).

[13] T. K. Gaylord and M. G. Moharam, "Analysis and applications of optical diffraction by gratings," Proc. of the IEEE 73, 894-937 (1985).

Chapter 6

[1] R. W. Wood, "On a remarkable case of uneven distribution of light in a diffraction grating spectrum," Phil. Mag. **4**, 396-408 (1902).

[2] S. S. Wang and R. Magnusson, "Theory and applications of guided-mode resonance filters," Appl. Opt. **32**, 2606-2613 (1993).

[3] L. Rayleigh, “On the dynamic theory of gratings,” Proc. Roy. Soc. **A79**, 399-416 (1907).

[4] A. Hessel and A. A. Oliner, “A new theory of Wood's anomalies on optical gratings,” Appl. Opt. **4**, 1275-1299 (1965).

[5] S. S. Wang, R. Magnusson, J. S. Bagby and M. G. Moharam, “Guided-mode resonances in planar dielectric-layer diffraction gratings,” J. Opt. Soc. Am. A **7**, 1470-1474 (1990).

[6] D. Rosenblatt, A. Sharon, and A. A. Friesem, “Resonant grating waveguide structure,” IEEE J. Quant. Electron. **33**, 2038-2058 (1997).

[7] H. Gao, J. M. McMahon, M. H. Lee, J. Henzie, S. K. Gray, G. C. Schatz and T. W. Odom, "Rayleigh anomaly-surface plasmon polariton resonances in palladium and gold subwavelength hole arrays," Opt. Express **17**, 2334-2340 (2009).

[8] A. T. M. Anishur Rahman, P. Majewski and K. Vasilev, "Extraordinary optical transmission: coupling of the Wood-Rayleigh anomaly and the Fabry-Perot resonance," Opt. Lett. **37**, 1742-1744 (2012).

[9] M. S. Amin, J. W. Yoon and R. Magnusson, "Optical transmission filters with coexisting guided-mode resonance and Rayleigh anomaly," Appl. Phys. Lett. **103**, 131106 (1-4) (2013).

[10] R. Magnusson, "Flat-top resonant reflectors with sharply delimited angular spectra: an application of the Rayleigh anomaly," Opt. Lett. **38**, 989-991 (2013).

[11] T. K. Gaylord and M. G. Moharam, “Analysis and applications of optical diffraction by gratings,” Proc. of the IEEE **73**, 894-937 (1985).

Biographical Information

Tanzina Khaleque completed her B.Sc. and M.Sc. in electrical and electronic engineering from Bangladesh University of Engineering and Technology (BUET), Dhaka, Bangladesh in 2006 and 2009 respectively. She was appointed as a lecturer in electrical and electronic department of BUET in 2006. She started her Ph.D. program at the department of electrical engineering in University of Texas at Arlington in Fall 2009.

In her M. Sc. thesis she analyzed DWDM transmission system performance considering gain saturation effect of semiconductor optical amplifier using MATLAB. Her B.Sc. thesis focuses on the analysis of performance limitations of a subcarrier multiplexed optical transmission system due to optical beat interference using MATLAB. In her Ph.D., she has worked with the analysis, design, fabrication and characterization of guided-mode resonant thin-film silicon solar cells and flat-top reflectors.

Tanzina's research interests include design and fabrication of efficient nano-structured thin-film solar cells and resonant GMR devices. She plans to continue her research involving cell-level and system-level design of photovoltaics and their implementation. Her goal is to find a research position in industry or academic institute to pursue her research career.